

**Technische Universität Berlin**

MSc Computational Neuroscience

Bernstein Center for Computational Neuroscience Berlin

Philipstr. 13, Haus 6

10115 Berlin

<https://www.bccn-berlin.de/>



Master Thesis

**Characterization and Classification of Finger  
Movement-Related Brain Activity using Optically  
Pumped Magnetometers**

Martin Iniguez de Onzono Muruaga

Matriculation Number: 0453088  
15.03.2024

Supervised by  
Prof. Dr. med. Surjo R. Soekadar  
Dr. Livia De Hoz  
Jan Zerfowski, MSc



Hereby I declare that I wrote this thesis myself with the help of no more than the mentioned literature and auxiliary means.

Berlin, 15.03.2024

.....  
*(Signature )*

[Martin  
Iniguez de  
Onzono Mu-  
ruaga]



## Abstract

Stroke significantly impairs upper limb function, directly affecting quality of life. Brain-Computer Interfaces (BCIs) processing brain signals to control external devices offer promising rehabilitation solutions. However, the spatial resolution limitations of the standard recording technique, electroencephalography (EEG), hinder the decoding of brain activity.

This research explores the use of magnetoencephalography (MEG) with Optically Pumped Magnetometers (OPMs), which provide higher spatial resolution, focusing on the potential for discriminating finger movements. By investigating the capabilities of OPM-MEG through frequency analysis, spatial filtering, and deep learning, this thesis aims to advance BCI technology, focusing on decoding finger movement-related neural activity.

Initial findings in this study hinted at potential for binary classification, particularly in the beta band (12.5 Hz to 30 Hz). Frequency-based analysis, focused on that band, underscored the difficulty in achieving reliable discrimination via visualization. Using more complex approaches, a notable outcome was achieved with a Low-Frequency Convolutional Neural Network (LF-CNN), revealing a classification accuracy of 76% between two specific finger movements. This result is comparable to state-of-the-art findings using EEG. Multi-class discrimination among five fingers, on the other hand, proved to be challenging since the differences in brain activity were too subtle.

The study shows that although OPMs provide high spatial resolution, their effectiveness in complex BCI tasks such as fine-grained finger movement discrimination remains limited. This highlights the necessity for additional research and the potential benefits of integrating OPM data with other modalities to improve classification performance.



## Gracias

No hay mejor manera de expresarse que en la lengua en la que uno piensa. Eso en parte ya simboliza mucho. El hecho de inmigrar, adaptarse a una nueva cultura, idioma, clima, costumbres. Es duro. Durante estos años de Máster, y en especial de tesis, me he visto envuelto en un sinfín de emociones, vivencias, momentos preciosos y también muy difíciles. Mi trabajo en recuperar mi cuerpo, tras una operación difícil y una situación mental complicada, ha estado llena de baches y de pequeñas victorias. Vamos en buena dirección, aunque será una lucha que, por suerte o por desgracia, me acompañe toda mi vida.

Hoy soy una persona muy distinta de aquel Martín que llegó a una torre inanimada en Lichtenberg y que tuvo que mantenerse cinco días sólo en una cuarentena. Qué rápido pasa el tiempo y cómo nos acostumbramos a los cambios. En el camino, he conocido partes de mí que desconocía y he enfrentado situaciones que en muchas ocasiones creía insalvables. No podría haber superado esos obstáculos sin todas vosotras.

Primero, me gustaría dar las gracias a la Fundación La Caixa por haber apostado por mí y darme esta oportunidad de oro. Gracias por vuestro apoyo. A mi tutor Jan por acompañarme en todo momento. A Surjo por acogerme en tu laboratorio. A mis compañeras de Máster, Anuja, Jana por haber hecho todo este esfuerzo más fácil y ameno. A mis compañeros de piso, por proporcionarme un hogar donde caer rendido. A Olga, por ayudarme a transitar mi mente. A los amigos que Berlín me ha regalado, Hugo, Alexia, Patricia, Eva, Valerie, Pablo, Julieta, Ana, Malou, Almudena, Luis ... A Paula, por ser un espejo y una canoa que admirar. A mi Gonzalo, por enseñarme que el mundo todavía es sensible y que las emociones y el cariño siempre serán lo más importante. A mi Campamento, desde la lejanía ofreciendo un faro que guía mi barco. A mi Andrés, farero por excelencia, capitán de las marejadas y sonrisa desde el Bósforo, te quiero amigo. A mi Lilith, por enseñarme de nuevo lo que es amar y ser amado. Ésto no hubiera sido posible sin ti, eres una de las almas más bonitas y puras que jamás conocí. Te quiero. A mis padres, que me dieron el mayor apoyo que un hijo pueda desear. Estuvisteis ahí cuando más os necesitaba, como siempre, y aún cuando no sabía que os necesitaba. Al compañero de viaje eterno que me ha acompañado, guiado y recomfortado durante todos estos años, en los cuáles hemos madurado juntos de la manita, abrazados como en nuestro sticker favorito. Franco, eres un tesoro. Y no me puedo olvidar de darme las gracias a mí mismo, por la generosidad con la que me he tratado, la calma que he encontrado por mi cuenta y la capacidad de reponerme ante tantas adversidades. Gracias Martín.

Por último me gustaría dar las gracias a la música, por haberme liberado de cuerpo y alma en tantos momentos. Como tantas veces a lo largo de toda mi vida, no sé que hubiera sido de mí sin ti.

Gracias a todas. Empieza una nueva etapa. Hay Martín para rato.



# Contents

<b>List of Figures</b>	<b>xi</b>
<b>List of Tables</b>	<b>xiii</b>
<b>List of Acronyms</b>	<b>xv</b>
<b>1 Introduction</b>	<b>1</b>
1.1 Motivation . . . . .	1
1.2 Literature Review . . . . .	2
1.2.1 Stroke . . . . .	2
1.2.2 Non-Invasive Recording . . . . .	3
1.2.3 Optically Pumped Magnetometers . . . . .	5
1.2.4 Brain-Computer Interfaces . . . . .	6
1.2.5 Finger Movement Discrimination . . . . .	6
<b>2 Methods</b>	<b>9</b>
2.1 Data Acquisition . . . . .	9
2.1.1 Experimental Setup . . . . .	9
2.1.2 Experiment Protocol . . . . .	11
2.2 Preprocessing . . . . .	11
2.2.1 Loading Data . . . . .	11
2.2.2 Creating the Necessary Variables . . . . .	12
2.2.3 Filtering . . . . .	12
2.2.4 Channel Selection . . . . .	12
2.2.5 Dividing Data into Epochs . . . . .	12
2.2.6 Manual Inspection . . . . .	13
2.3 Analysis and Classification . . . . .	13
2.3.1 Channel Selection . . . . .	13
2.3.2 Spatial Filtering . . . . .	15
2.3.3 CSP on Beta-Band . . . . .	15
2.3.4 Frequency-based Analysis . . . . .	16
2.3.5 Deep-Learning Approaches . . . . .	18
<b>3 Results</b>	<b>23</b>
3.1 Time-Frequency Representation . . . . .	23
3.2 Synchronization Frequency Power . . . . .	24
3.3 Beta Power over Time . . . . .	24

3.4	Beta Power across all Sensors . . . . .	25
3.5	CSP on Beta-Band . . . . .	26
3.6	Finger Discrimination Classification . . . . .	27
<b>4</b>	<b>Discussion</b>	<b>31</b>
<b>5</b>	<b>Limitations</b>	<b>35</b>
<b>6</b>	<b>Conclusion and Next Steps</b>	<b>37</b>
	<b>Bibliography</b>	<b>39</b>
	<b>Annex</b>	<b>45</b>
.1	Availability of the Source Code . . . . .	45
.2	Extra Figures . . . . .	46

# List of Figures

1.1	SQUID-MEG. . . . .	4
1.2	Optically Pumped Magnetometer. . . . .	5
1.3	OPM physics. . . . .	8
2.1	Experimental setup. . . . .	10
2.2	Finger drawings shown to the participant. . . . .	11
2.3	Sensors' 2D map projection. . . . .	14
2.4	DeepConvNet Architecture. . . . .	20
2.5	LF-CNN Architecture. . . . .	21
3.1	Time Frequency Representation for different states. . . . .	23
3.2	SFP for 5 different channels. . . . .	25
3.3	Beta Power over time. . . . .	26
3.4	Beta Power across all sensors. . . . .	29
3.5	CSP on beta band. Finger 3 vs Finger 5 comparison. . . . .	30
.1	TFR for different states for HI[X] channel. . . . .	46
.2	TFR for different states for FW[X] channel. . . . .	46
.3	TFR for different states for FY[Y] channel. . . . .	47
.4	TFR for different states for HQ[Z] channel. . . . .	47

*Characterization and Classification of Finger Movement-Related Brain Activity using  
Optically Pumped Magnetometers*

## List of Tables

3.1 Binary classification accuracy results. . . . .	28
---	----

*Characterization and Classification of Finger Movement-Related Brain Activity using  
Optically Pumped Magnetometers*

# List of Acronyms

BCI	Brain-Computer Interface
EEG	Electroencephalography
MEG	Magnetoencephalography
OPM	Optically Pumped Magnetometer
ERF	Event-Related Field
MIT	Motor Imagery Training
rTMS	Repetitive Transcranial Magnetic Stimulation
ECoG	Electrocorticography
SQUID	Superconducting Quantum Interference Device
MSR	Magnetically Shielded Room
SERF	Spin-Exchange Relaxation Free
MIT	Motor Imagery Training
ERS/ERD	Event-Related Synchronization/Desynchronization
SMR	Sensorimotor Rhythms
CNN	Convolutional Neural Network
ELU	Exponential Linear Unit
ReLU	Rectified Linear Unit
LF-CNN	Linear Finite-Impulse-Response Convolutional Neural Network
SNR	Signal-to-noise ratio
CSP	Common Spatial Patterns
LDA	Linear Discrimination Analysis
TFR	Time-Frequency Representation
SFP	Synchronization Power Frequency



# 1 Introduction

## 1.1 Motivation

Stroke, one of the leading causes of disabilities around the world (“Impact of stroke”, 2024), is known to cause upper limb impairment, affecting directly the quality of life of individuals that suffer from it (Hussain et al., 2018). Brain-Computer Interfaces (BCIs), systems that use brain signals to control external devices (like exoskeletons or computers), are one of the most prominent techniques to help during stroke rehabilitation (S. R. Soekadar et al., 2015; Nann et al., 2021).

Currently, the standard method to record neural activity to control BCIs is electroencephalography (EEG). However, it has been seen that EEG’s spatial resolution is very low to detect subtle differences between neighbouring areas in the brain due to a phenomenon called volume conduction (Vaid et al., 2015).

Magnetoencephalography (MEG) is the alternative to EEG for non-invasive recording techniques with high temporal resolution. Its physical foundation relies on capturing the magnetic fields originating from the brain’s electrical currents (Singh, 2014). The advantage of MEG is that it provides considerably better spatial resolution than EEG. That is the case because MEG does not suffer from volume conduction and the decay of field over distance is stronger (Seymour et al., 2022).

The conventional way to record MEG is Superconducting Quantum Interference Device (SQUID)-based MEG. However, this method involves very static and expensive setup, requiring cryogenic cooling systems and a fixed big structure to acquire the data (Hari & Salmelin, 2012). SQUID-BCI has also been studied and showed to work. However, SQUID-BCI lacks the mobility a BCI would require for its widespread use (Mellinger et al., 2007). Optically Pumped Magnetometers (OPMs), on the contrary, are mobile and they do not require such expensive equipment (Pedersen et al., 2022).

Research on OPM-BCIs is still very limited and therefore further examination and analysis is required to unveil the true power of this method. Paek et al. (2020), Zerfowski et al. (2021), Fedosov et al. (2021), Zerfowski (2022), and Wittevrongel et al. (2021) are ones of the only studies investigating this matter. None of them explored the concept of finger movement discrimination using OPM data.

The motivation behind this thesis lies on exploring the field of OPM-BCIs, specifically to learn whether finger movement discrimination is achievable using them. Event-Related Fields (ERFs) from the motor cortex were assessed to perform such discrimination.

Decoding finger movements has already been attempted with EEG, but the results were still not satisfactory enough for implementation into a BCI paradigm (Liao et al., 2014). This thesis proposes that due to OPM-MEG having more sensors and better spatial

resolution compared to EEG, it may outperform EEG-based methods in classification tasks.

This study serves as a preliminary investigation to find the strengths and weaknesses of OPM-MEG neural decoding. As a result, we only conducted offline classification. That means that the objective was not finding a way to control a BCI with finger independence, but to discover whether there is any difference in brain activity when different fingers move.

To investigate these differences, several analyses centered around frequency, particularly emphasizing the beta band (12.5 Hz to 30 Hz), were conducted. Spatial filtering techniques along with deep learning approaches were also employed to tackle this research question from a varied set of perspectives.

## 1.2 Literature Review

### 1.2.1 Stroke

Stroke is one of the leading causes of death and disability in the world. Over 100 million people are estimated to have experienced stroke and over 12 million more will suffer their first one this year (“Impact of stroke”, 2024). From an economic perspective, it is estimated that nearly 5% of total healthcare expenditure in industrialised countries is associated to the medical costs of stroke patients (Benesch & Holloway, 1998).

Between 1 and 4% of people that have had a stroke developed a movement disorder (Handley et al., 2009), and the prevalence of upper limb impairment is approximately 50–80% in the acute phase, and 40–50% in the chronic phase (Hussain et al., 2018).

Intravenous thrombolysis is crucial when administered in an acute ischemic stroke (Prabhakaran et al., 2015) but rehabilitation is also crucial after the first stages of the stroke. There is a wide range of treatments used to re-gain some of these upper limb motor functionalities (Kim, 2022), e.g. constraint-induced movement therapy (Wolf et al., 2006). However, 30–50% of stroke survivors lose the capability of exerting voluntary movement, which renders some of these treatments inapplicable (Ushiba & Soekadar, 2016).

Some other rehabilitation techniques like motor imagery training (MIT) (Stockley et al., 2021), or repetitive transcranial magnetic stimulation (rTMS) (Meng et al., 2020), have been used to target this issue.

Another approach, which is the target of this master thesis, is the use of exoskeletons during rehabilitation via BCIs. BCIs are systems used to translate cortical signals into control signals of external devices, such as a computer or a prosthesis (Nicolas-Alonso & Gomez-Gil, 2012). It has been seen that the use of BCI-controlled exoskeleton can even help restoring daily-life activities after quadriplegia (S. Soekadar et al., 2016), and stroke (Mane et al., 2020).

However, to be able to control these BCIs, cortical activity needs to be recorded. There are various methods to do so, being the most accurate and precise the recordings performed invasively, i.e. recording directly from the brain tissue and thus, having to open a

# *Characterization and Classification of Finger Movement-Related Brain Activity using Optically Pumped Magnetometers*

hole in the skull (Hnazaee et al., 2022). One established way to do so is electrocorticography (ECoG), which produces better results than any non-invasive technique so far, even when complex computational post-processing is involved (Graimann et al., 2005).

## **1.2.2 Non-Invasive Recording**

Performing invasive recordings requires neurosurgery and insertion of an implant inside the skull. This is still frowned upon by the medical community (Waldert, 2016). The risks are evidently not insignificant but appear to be somewhat exaggerated though (Zrinzo et al., 2012). That is the reason non-invasive BCIs prevail to this date.

BCIs require high temporal resolution due to the rapid and dynamic nature of brain activity. Real-time decoding of neural signals is needed to enable a direct interaction between the brain and external devices (Ordikhani-Seyedlar et al., 2016).

To this date, EEG is the standard non-invasive recording technique with high temporal resolution. EEG measures the electrical signals generated by groups of neurons in the brain, which fire together in a synchronized manner. These signals are captured using electrodes that are positioned on the scalp (Light et al., 2010).

It is widespread used due to its low cost, high temporal resolution, portability, and how easy it is to be operated. This makes it ideal for capturing the brain's rapid dynamical changes and translating them into commands for controlling external devices or software (Abiri et al., 2019). However, EEG has also its problems. The signal quality is often compromised by various types of interference, such as muscle movements, external electrical noise, and the phenomenon of volume conduction, where electrical currents spread across the scalp, resulting in a signal with a low spatial resolution (Vaid et al., 2015).

The other non-invasive recording technique available to this date with a high temporal resolution is MEG, which captures the magnetic fields generated by the electrical currents of the brain (Singh, 2014). Within the spectrum of signals that MEG captures, ERFs are the ones of the most interest for this thesis. ERPs are magnetic responses that occur in direct relation to specific cognitive or sensory events, serving as a window into the neural processes that underpin these events (Pfurtscheller & Da Silva, 1999).

MEG presents a big advantage in comparison to EEG; it has a higher spatial resolution, since magnetic fields are not distorted by the electrical conductivity of scalp, cerebrospinal fluid, brain and skull. That means source localization can be done with a 2-3 mm spatial resolution, in comparison to the 7-10 mm resolution of EEG (Singh, 2014). Also, due to the cubic decay of magnetic fields with distance to the source, little to no muscle artifacts are expected in OPM data (Seymour et al., 2022).

On the other hand, it poses a big disadvantage in terms of its use in different environments. It requires a magnetically shielded room (MSR) to record any data. That is the case because the Earth's magnetic field ranges from 30 to 60 microtesla ( $\mu\text{T}$ ), while the magnetic fields coming from the brain appear in the range of pico- to femtoT (Hari & Salmelin, 2012). <sup>1</sup>

---

<sup>1</sup>In the International System of Units (SI), prefixes represent powers of ten. Micro ( $\mu$ ) denotes  $10^{-6}$ , nano ( $n$ ) denotes  $10^{-9}$ , pico ( $p$ ) denotes  $10^{-12}$  and femto ( $f$ ) denotes  $10^{-15}$ .

*Characterization and Classification of Finger Movement-Related Brain Activity using Optically Pumped Magnetometers*

Currently, the main modality of MEG recording is SQUID-MEG. There are nevertheless three big disadvantages for this modality of MEG.

- The first one is its dependence on superconductance, meaning that the sensors must remain in very cold temperatures, close to 0K (-273°C). Thus, a very expensive and massive structure needs to be built and maintained (Hari & Salmelin, 2012).
- The second one would be that SQUID-MEG requires the subject to be in a fixed position. The structure containing the sensors is fixed in a rigid position. Recording while doing active tasks involving the movement of the subject is challenging (Boto et al., 2018).
- The last one would be that SQUID-MEG helmet cannot be customized to the shape of the head of the participant. There is only the possibility of using a one-size-fits-all type of helmet, as seen in the Fig. 1.1 (Boto et al., 2017).



Figure 1.1: **SQUID-MEG**. Subject being recorded by a SQUID-MEG. Figure extracted from Boto et al. (2018).

### 1.2.3 Optically Pumped Magnetometers

Optically Pumped Magnetometers (OPMs)-MEG solve the three problems described above. They do not rely on cryogenic cooling, therefore making any recording much cheaper and the equipment much easier to maintain (Pedersen et al., 2022). OPMs can be attached to a portable helmet, allowing for movement of the participants and enabling them to stay in more comfortable positions in which they can perform active tasks (Brookes et al., 2022). Lastly, a bespoke helmet can be constructed based on the participant's structural MRI data, incorporating precise sensor placements. This approach offers an additional level of customization, ensuring optimal fit and alignment with the individual's brain structure (Boto et al., 2017). A picture of a commercial OPM can be appreciated in Fig. 1.2.



Figure 1.2: **Optically Pumped Magnetometer.** Image extracted from “Optically Pumped Magnetometers from QuSpin Guide Drones & Brain Imaging” (2024). Accessed February 6, 2024.

OPMs' functionality relies on the quantum property of atomic spin- both nuclear and electron spin- to detect local magnetic fields (Kastler, 1951). Each OPM unit is formed by a glass cell containing an atomic vapour from an alkali metal, a laser with associated optics to project polarized laser light through the cell, and a photodiode for detecting the light that passes through the atomic vapour. Once these atoms are “pumped” by the laser into a specific quantum state, the atomic vapour is magnetised. That magnetization induces the vapour to interact with any external magnetic field present, like the one created by the brain electrical current. These interactions cause variations in the amount of light that eventually passes through the vapor, and a photodiode at the end of that can be used to infer the magnitude of this magnetic field (Brookes et al., 2022). The scheme in Fig. 1.3 represents how this process works.

After decades of OPM improvements in size (miniaturization) and making them cheaper and more accessible, the spin-exchange relaxation free (SERF) regime OPMs appeared, exhibiting a higher sensitivity than traditional OPMs (Allred et al., 2002).

This regime requires temperatures of around 150°C, but thanks to thermal insulation, the sensors can be placed just a few millimetres from the scalp, compared to the 2 or more cm in SQUID-MEG. This provides a signal enhancement of 4 to 5 times in terms

## *Characterization and Classification of Finger Movement-Related Brain Activity using Optically Pumped Magnetometers*

of signal-to-noise ratio (SNR) in many cortical areas, as well as presenting less muscle-related movement artifacts (Boto et al., 2016; Ilivanainen et al., 2017; Boto et al., 2018).

### **1.2.4 Brain-Computer Interfaces**

Invasive recording techniques, like ECoG, show undoubtedly the best results for BCI control (Schalk & Leuthardt, 2011). However, as stated earlier, EEG is the most widespread recording technique for the use of BCI nowadays. It relies on the appearance of event-related synchronizations/desynchronizations (ERS/ERD), i.e., modulations in the sensorimotor rhythms (SMR). These modulations tend to occur in the alpha and beta bands (8 Hz to 12 Hz and 12.5 Hz to 30 Hz respectively) during/after the cognitive processing of an event (Neuper et al., 2006).

These ERDs can be induced by voluntary movement (Toro et al., 1994) and motor imagery (Jeon et al., 2011). Participants can learn to modulate these rhythms using real-time neurofeedback and proper training (Weber et al., 2011). Apart from these bands, the gamma band (30 Hz to 60 Hz) has also been found to be related to the execution and control of fine movement (Jia and Kohn, 2011; Ulloa, 2022).

For BCIs controlling upper limb movement, the motor cortical areas known by EEG location convention as C3 (left) and C4 (right) are the most important (Cobb et al., 1958). Body movement is controlled contralaterally, that means we control the movement of the right arm with our left motor cortex. Thus, C3 controls the right hand movement.

Using the same paradigm as for EEG (looking for modulations in the SMRs), controlling BCIs using SQUID-MEG has also been tried (Mellinger et al., 2007). ERD and ERS phenomena are not only found with EEG, but also within SQUID-MEG recordings, following for instance finger, toe or mouth movements (Salmelin et al., 1995). It has been seen that MEG has a higher spatio-temporal resolution and robust spatial filtering methods, which can reduce the computational load and improve classification, in comparison to EEG (Lin et al., 2013). The lack of portability and higher costs of SQUID-MEG makes it hard for any takeover on the EEG standard though.

That is an issue that OPM-BCIs would target. OPM-BCI control has already been tried but very few publications have been released so far. Paek et al. (2020) had very poor results applying it and did not perform online classification but only offline, with a task involving classification of move or rest states. Fedosov et al. (2021) also worked on motor imagery (grasp versus relax) in an online classification manner, with only one single trained participant. Zerfowski (2022) showed a significant difference in SMR power between resting and grasping conditions on 10 participants, exceeding significantly chance level in classification. It has also been applied in non-movement related tasks like spelling, with very high accuracy (Wittevrongel et al., 2021).

### **1.2.5 Finger Movement Discrimination**

Grasping and relaxing are still very simple tasks, which do not fully reflect how we use our hands in our daily basis. For that reason, decoding how the brain activity looks

*Characterization and Classification of Finger Movement-Related Brain Activity using  
Optically Pumped Magnetometers*

when different fingers move is the mandatory next step to provide an even better quality of life to people in need of BCIs (Shin et al., 2009).

Quandt et al. (2012) showed a comparison between how SQUID-MEG and EEG can classify finger movements on single trial discrimination using Support Vector Machines (SVMs), having a 57% average accuracy for MEG and 43% for EEG (chance level being 25%). When performing finger-to-finger discrimination (performing binary classification multiple times among pairs of fingers), results for SVMs on EEG data show a decoding accuracy of 77% and a very high 91% using ECoG (Liao et al., 2014).

The rise of deep learning as a classification tool has also reached this field of research and many studies have been done using this approach. Schirrmeister et al. (2017) developed a complex deep convolutional network (DeepConvNet) to classify between hands (left or right), feet movement or resting condition on EEG data- showing 84% accuracy on a 4-class classifier. Simpler convolutional networks, like LF-CNN, were also able to distinguish between left, right hand movement or no movement on SQUID-MEG signals (Zubarev et al., 2019)- with an 86% accuracy on a 3-class classifier.

Bu et al. (2023), used deep convolutional networks to differentiate between different hand gestures in a rock, paper, scissors experiment- 33% chance level. 86% classification accuracy was attained on SQUID-MEG. All these deep learning approaches convey an important disadvantage. Due to their heavy reliance on time and computational resources, they are not suitable for online classification. As a result, they cannot provide the instantaneous feedback control required for effective operation of a BCI.

Finger discrimination presents significant difficulty, particularly as it has yet to be explored with OPMs. Consequently, our study focused exclusively on offline techniques. This step creates the groundwork for subsequent application to online scenarios, and ultimately, BCI control.

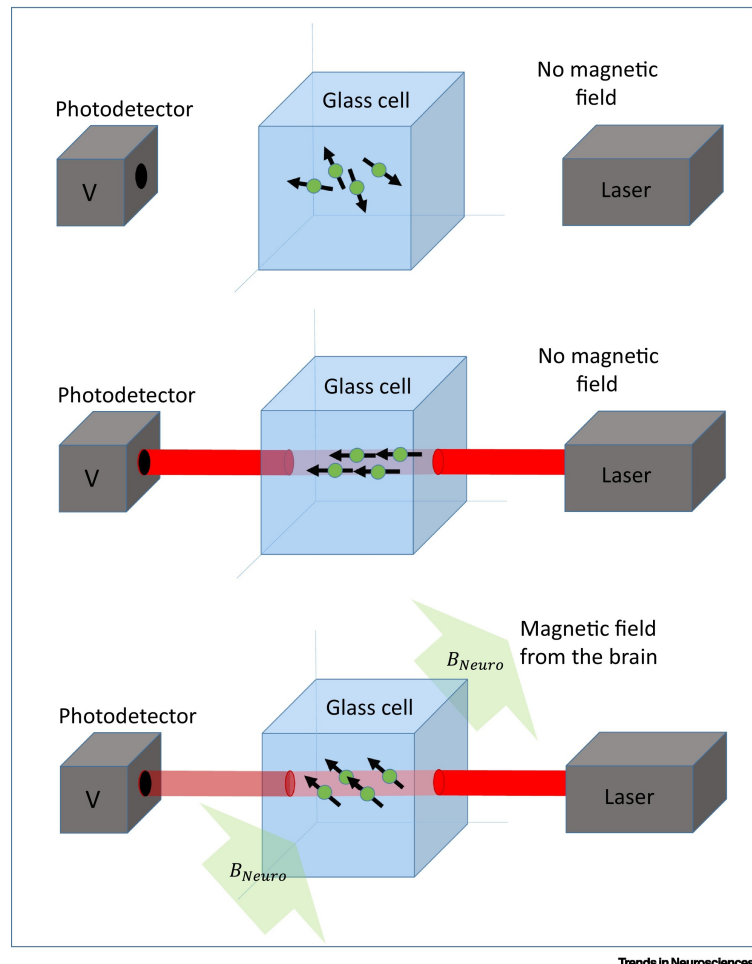


Figure 1.3: **OPM physics.** Diagram showing how the alkali metal vapour interacts with the photons from the laser, modulated by a magnetic field. Image extracted from “Optically Pumped Magnetometers from QuSpin Guide Drones & Brain Imaging” (2024).

## 2 Methods

### 2.1 Data Acquisition

This section outlines the data acquisition process in our study. This concise overview focuses on the collaborative efforts, equipment usage, and participant tasks involved in acquiring the data, offering clarity on the methodology used.

#### 2.1.1 Experimental Setup

The experiment was recorded as part of a visit on 21-23.03.2023 at Professor Matthew J. Brookes' laboratory, at the Sir Peter Imaging Centre at University of Nottingham. The recording was performed in collaboration with Dr. Elena Boto, Dr. Ryan, Holly Schofield, and Professor Matthew J. Brookes. An MSR located within that facility was used for the recording. The experimental paradigm was developed by Jan Zerfowski.

The data were recorded using QuSpin's (Louisville, Colorado, USA) Neuro 1 OPM-system with 65 triaxial (i.e., 3 orthogonal channels/axes per sensor) sensors available (meaning 195 total available channels). The OPM used can be seen in Fig. 2.1A.

The participant entered the room and sat down in a chair situated in front of a table on which the button-pressing devices were located. A bespoke OPM helmet – based on their structural MRI with known relative sensor locations – was used. It was designed following similar guidelines as the ones explained in Boto et al. (2017).

A patch with a higher density of sensors was placed upon the left motor cortex – also known in the 10/20 EEG system as C3 (Cobb et al., 1958). This region was chosen because it is widely acknowledged as the primary cortical area responsible for right-side motor execution (see Fig. 2.1 B). In the end, 55 sensors were used, making the total of channels 165 (X, Y and Z dimensions).

To register button presses during the experiment, an MEG/MRI-proof, non-magnetic button was used (Current Designs, Philadelphia, Pennsylvania, USA) ("Current Designs button boxes", 2024). Stimuli were shown on a tilted rear projection screen using a projector located outside the shielded room. The screen was positioned at an approximate distance of 1 meter from the subject. The whole experimental setup can be seen in Fig. 2.1 C.

Fingers will be referred to from now on as number 1 to number 5, following the logical thumb, index, middle, ring and little finger order.

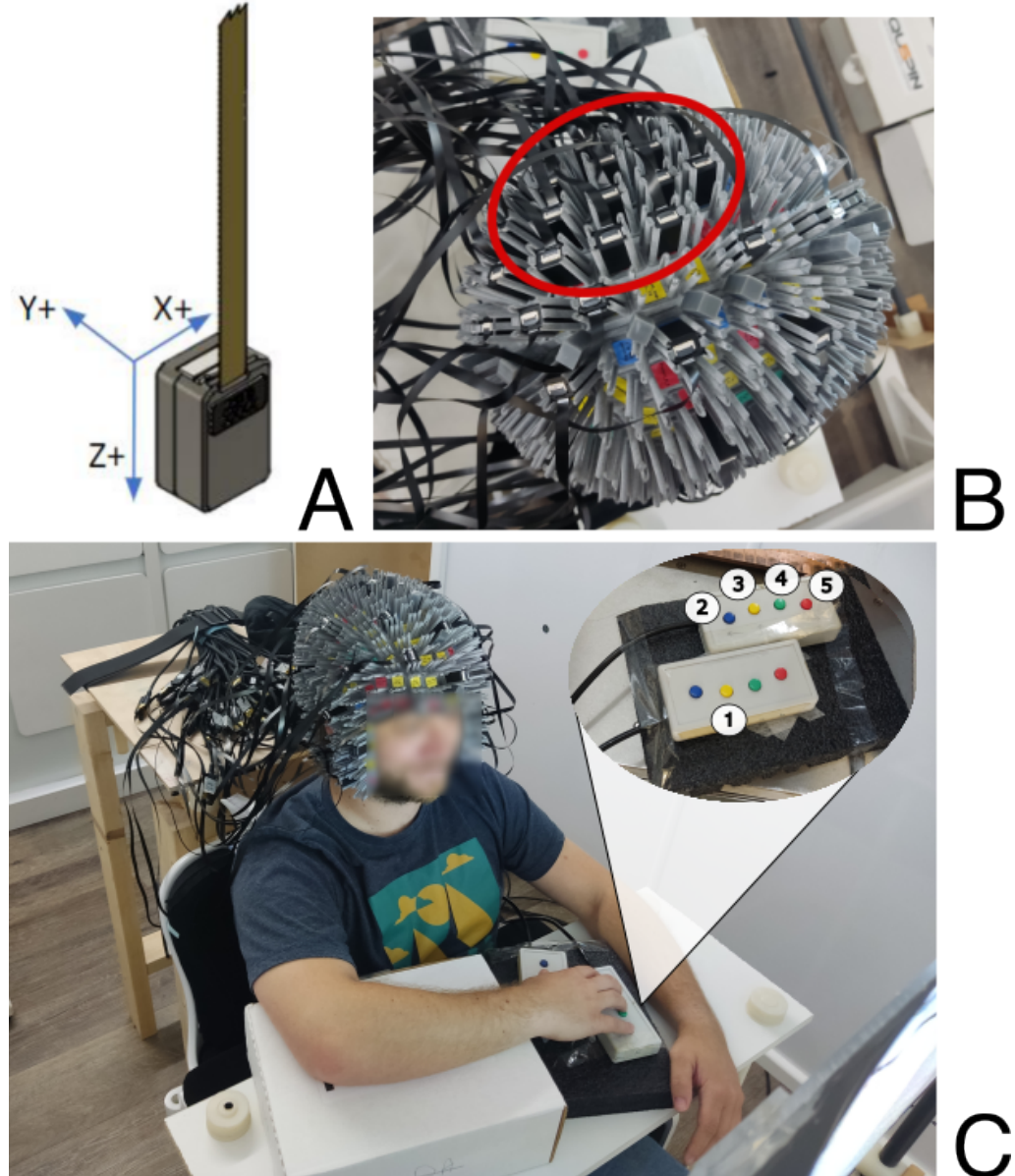


Figure 2.1: **Experimental setup.** **A).** QuSpin OPM sensor, containing three recording channels (X, Y and Z). Image extracted from “QZFM Dimensions” (2024). **B).** Area from bespoke helmet having a higher density of sensors (C3, left motor cortex). **C).** Picture showing the experimental setup used. The participant had those two button-pressing devices set up in a table in front, which had to be pressed with the pattern displayed in the Figure. The yellow button on one device corresponded to the thumb, and on the other device: blue to index, yellow to middle, green to ring, and red to little finger.

### 2.1.2 Experiment Protocol

5 recordings were acquired, each with a sensor zeroing and a brief break in between. The participant was asked to move as little as possible while the recordings took place. The door to the MSR remained closed during the breaks and the participant did not execute any big movements.

The recordings lasted 7 minutes, in which 100 epochs of 4.16 seconds occurred. One of the recordings appeared to be corrupted and was not included in the study. Thus, the total amount of epochs included in the analysis was 400 (100 per recording).

Each epoch started by showing a cue in the screen placed in front of the participant. To display them in the MSR, the experiment was translated into a MATLAB *.m-file* implementing the stimulus presentation. That image took one of the 5 different forms appearing in Fig. 2.2, showing which finger should be doing the button press. In this interval, the participant had to press the correct button represented by a finger in the screen. After 2.1 seconds of continuous presentation of the cue, the image would disappear for 2.06 seconds, and the participant would rest until the start of the next epoch.

After the experiment concluded, a final recording of resting data was captured, while which the participant remained seated and still. It should be noted that there was a construction site close to the building, which sometimes added some broad band noise. The noise should be relatively spatially uniform within the MSR but occurred mainly only during the resting recording.

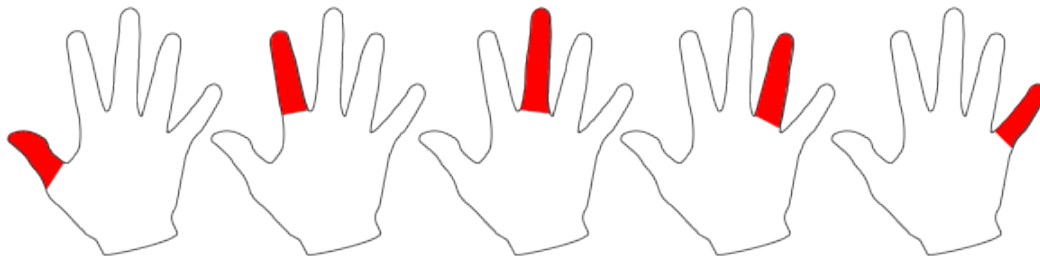


Figure 2.2: **Finger pictures shown to the participant.** Drawings shown to the participant to indicate which finger should be moved.

## 2.2 Preprocessing

The following steps were carried out to identify any artifacts or periods of higher noise within each recording individually.

### 2.2.1 Loading Data

The data was recorded originally in a *cMEG* file. A script provided by the Nottingham group was used to read the data from this binary format, using a file header to determine the dimensions of the array. The information corresponding to the channels, the

configuration of the helmet, the transformation matrices needed for the sensors were all extracted from *TSV* files containing such information for each individual recording. An additional *JSON* file contained the last bits of information needed for the preprocessing, such as the power line frequency and the sampling frequency.

### **2.2.2 Creating the Necessary Variables**

With all these data, a raw data object was created, channels were configured (location, scale, type and orientation) and events were created. These events contained both the cue and pressing of buttons, as well as the end of the epoch and the end of the recording. Another step was taken to eliminate any mistrials, i.e. epochs in which the correct finger tap was not achieved. There were three types of errors: either another button was wrongly pressed, two buttons were pressed in the same epoch, or no button was pressed at all.

MNE-Python functions were used to perform the next preprocessing steps. For that reason, an *mne.RawArray* was created, containing all events and markers as *mne.Annotations*.

### **2.2.3 Filtering**

A copy of the raw data was created, and an IIR, zero-phase, 4th order Butterworth (non-causal) notch filter was applied at 50 Hz, which corresponds to the power line frequency. Another zero-phase, 4th order Butterworth IIR band-pass (0.01 Hz to 120 Hz) was subsequently applied to the data to remove the DC offset and unwanted high-frequencies, which hold no relevant information to us.

### **2.2.4 Channel Selection**

Given the nature of OPMs, there were sensors with 3 different magnetic axes (*X*, *Y* and *Z*), which were treated separately to select which channels to include in the analysis. For each dimension individually, all the channels' peak-to-peak amplitude was extracted. Then, z-scores of these peak-to-peak amplitudes within their respective distributions were calculated.

Channels with an absolute z-score value greater than 1.5 (whether negative or positive) in their peak-to-peak amplitude were discarded. This approach helped eliminate channels with either too low amplitude, indicating a very low SNR, or too high amplitude, suggesting that there was a high probability for the channel to be faulty or contain artifacts.

### **2.2.5 Dividing Data into Epochs**

The button presses were defined as the time 0 s of each epoch. 2 s were taken to each side of that point (+2 s and -2 s from that time point) to define every trial, creating epochs of 4 s.

To define the baseline interval within each epoch, representing the period of expected baseline neural activity, we calculated the average time from cue presentation to button

press across all epochs. That provided a standardized reference for identifying the baseline period in each recording. It yielded a mean time of  $(-0.57 \pm 0.08)$  s, which was used as the endpoint for the baseline.

The cue appears on screen for 2.1 s, followed by an absence period of 2.06 s. This creates a 0.16 s window, equivalent to twice the standard deviation of the calculated endpoint of the baseline, ensuring that the epochs do not overlap. That allows us to set the start of the baseline to the very start of the epoch (-2 s), resulting in a baseline for all epochs of -2 s to -0.57 s.

### 2.2.6 Manual Inspection

After this step, all the recordings were manually inspected with MNE's *RawArray.plot()* function using windows of 20 s. Transient jumps exceeding 30 picoTesla (caused by noise or movement artifacts) were flagged. Consequently, epochs containing these jumps were labeled as "bad" and subsequently excluded from the analysis.

The *mne.RawArray* and corresponding *mne.Epochs* objects were saved into a directory with each individual recording. The 4 successful recordings underwent this whole preprocessing pipeline individually.

## 2.3 Analysis and Classification

To identify differences among various states – specifically, button presses from different fingers – a set of diverse approaches was employed. The epochs from the 4 recordings were concatenated into a large 'epochs' variable, containing 388 epochs (due to 12 of them being mistrials), with a distribution of 78, 76, 77, 79, and 78 epochs for fingers 1 to 5, respectively.

### 2.3.1 Channel Selection

To perform some analysis and visualization, 5 different channels were chosen to show in the figures, since it would be very difficult to show the responses on all of them.

The sensor LQ, located on the center of the high-density patch on top of that C3 area, was chosen to be the "**C3 center channel**", and can be referred as such from now on. Looking at all 3 dimensions of the data acquired in that channel (X, Y and Z), the dimension X shown the highest signal amplitude, so LQ [X] was chosen as this C3 center sensor.

The analysis was based on the hypothesis that classification of different button presses could be achieved thanks to subtle variances between adjacent sensors in the C3 area. Neighboring sensors to LQ[X], FX[X] and HI[X], were selected to monitor these signal modulations. They will be referred also as **C3 electrodes**.

To show how the recorded activity looks in other directions and different positions, sensors with high amplitude in directions Y and Z were also selected: FY [Y] and HQ [Z]. In Fig. 2.3, the location of all sensors can be seen, with the five of most interest for the study highlighted.

## Characterization and Classification of Finger Movement-Related Brain Activity using Optically Pumped Magnetometers

Some sensors in the plots lie out of the head drawing. That comes from the inherent challenges of projecting sensors from a 3D space into a 2D figure. If the sensors were just projected to fit in the head drawing, the highly dense area of sensors would be very difficult to represent: all of them would lie on top of each other.

The figure was produced using MNE's `plot_sensors`. The `sphere` attribute of the function was used to define the radius of the sphere to which the sensor positions were projected onto. After trying different values, 0.12 was used since it was the one that looked the best. That radius will be used for all plots showing 2D projections of the sensors.

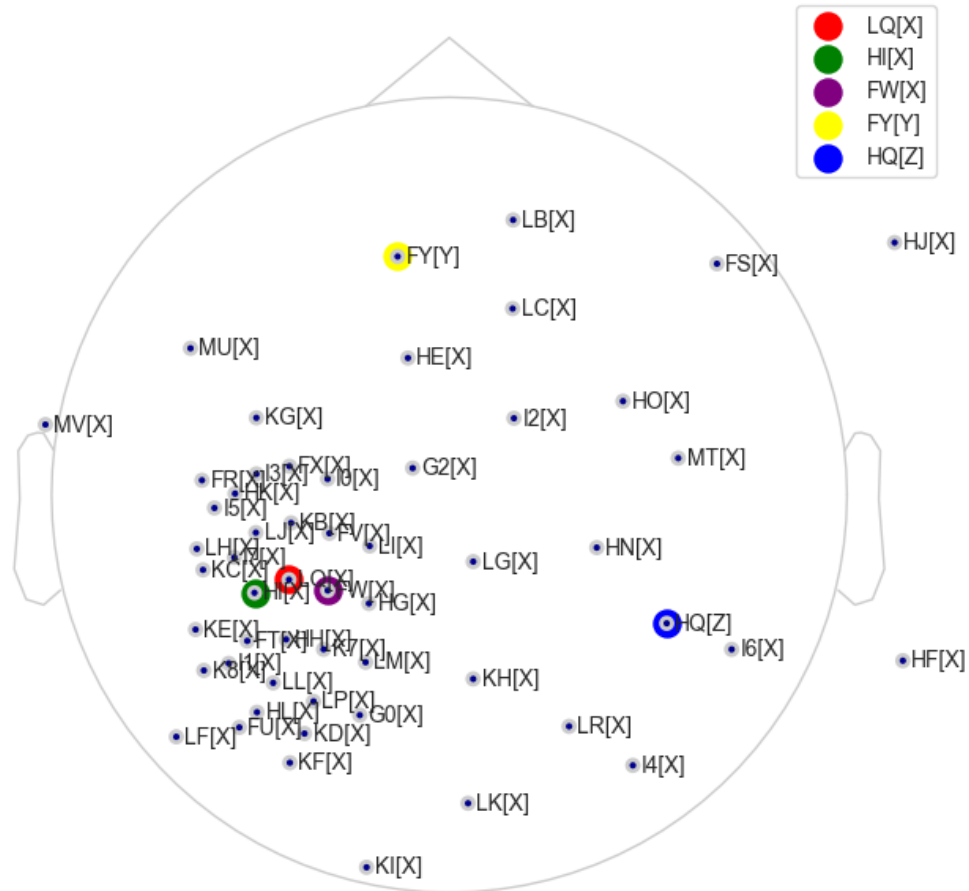


**Figure 2.3: Sensors' 2D map projection.** Sensors' location on the scalp. 2D projection, with the sensors of interest being highlighted (LQ, HI, FW, FY and HQ). Each sensor contains three channels (X, Y, and Z), with overlapping positions to one another.

### 2.3.2 Spatial Filtering

Dealing with a high number of channels for signal classification can be challenging. To simplify this, spatial filtering techniques like Common Spatial Patterns (CSP) are employed, specially in BCIs and EEG signal processing.

CSP is based on a simple principle: maximizing the variance of the signal pertaining to one class while minimizing the variance of a signal from another class. This approach effectively identifies spatial patterns in the data that are most informative for distinguishing between different brain states or activities.

This method is particularly useful in BCI applications because signal variance is a reliable measure of signal strength within specific frequency bands. By analyzing how the power within these bands varies across different locations, signals belonging to different classes can be effectively distinguished.

To solve this optimization problem, a generalized eigenvalue problem involving the covariance matrices of both classes must be addressed. The expression  $|\lambda - 0.5|$ ,  $\lambda$  being the eigenvalue of the CSP, must be maximized. The higher that expression is, the more effective the spatial filter is at distinguishing the two classes. That means that if the eigenvalue is close to 0.5, the spatial filter cannot effectively differentiate between states (Lotte & Guan, 2010).

As a result of solving this optimization problem, different components (or eigenvectors) arise, with an associated eigenvalue showing how good applying that filter differentiates between classes. They are orthogonal to each other and capture different information or features from the signal, emphasizing activity in different brain regions or aspects of the signal itself.

This was performed using MNE's *CSP* function. Then, once the CSP object has been fitted to the training data, the filters can be applied to transform the signal to the filter space, and the power of the signal for each filter can be computed for each epoch. Since 4 was the number of components used, each epoch has 4 features associated to them.

This set of features was used, along with Linear Discrimination Analysis (LDA), to classify signals between different states – like binary classification among finger presses. LDA is a statistical technique that projects the data onto a lower-dimensional space to maximize the variance across classes and minimize the variance within the same class. A 5-fold cross-validation paradigm with a 80/20 split (train and test data) was used to ensure the robustness of the results.

### 2.3.3 CSP on Beta-Band

As explained, to assess the discriminability between states in a MEG signal, CSP can be applied to the band-passed signal. This method evaluates whether the classes can be differentiated based on their variance within the specific frequency band. Knowing that the modulations of beta band (12.5 Hz to 30 Hz) are important ERS/ERD indicators (Neuper et al., 2006), it was decided to look at the CSP on the band-passed signal on the beta band.

The *CSP* function from MNE was executed for directions X, Y and Z, in order to find

the spatial filters corresponding to each dimension separately. CSP shows the differences between two classes. Thus, for each direction, the algorithm was run for all possible comparisons among fingers (binary classification), resulting in 10 different comparisons.

The *CSP* object's *patterns* attribute was visualized on a scalp diagram. This depiction illustrates the creation of spatial filters, revealing the channels assigned higher or lower weights for each filter. This visualization used a *sphere* radius of 0.12 for depicting electrode positions.

These spatial patterns- not to be confused with spatial filters- represent the spatial distribution of the activity that contributes to each spatial filter. The weight or coefficient assigned to each channel in these patterns indicates the importance of influence of that channel's data in the resulting spatial filter. A higher absolute value of the weight indicates that the channel's signal is more influential in distinguishing between the conditions.

The patterns of the first two components were plotted, i.e., the weights of the two spatial filters with highest differentiability among classes. Next to them, the eigenvalue associated to them was pointed out, which, as explained before, is an indicator of classification accuracy.

#### **2.3.4 Frequency-based Analysis**

Since a lot of the information hold in neural activity is "hidden" within the frequency domain, an extensive frequency-based analysis was carried out.

##### **Time-Frequency Representations**

For this purpose, Time-Frequency Representations (TFRs) were computed using Morlet Wavelet Transforms, utilizing the *tfr\_morlet* function from MNE-Python. TFRs shows how the frequency content of a signal changes over time. It provides insight into both the timing and frequency characteristics of the signal simultaneously.

Wavelet Transform is a method for analysing the frequency content of a signal over time, yielding a three-dimensional representation: time on the x-axis, frequency on the y-axis, and a colour scale (ranging from blue to red in our case) indicating the magnitude of the wavelet coefficient at each time and frequency. This magnitude reflects the similarity between the signal and the wavelet at that specific frequency and time (Prochazka et al., 2008).

This method was chosen over others like sliding window Fast Fourier Transform because it provides time-frequency localization, offers adjustable resolution, and uses basis functions specifically suited to capturing the dynamics of signals that have time-varying features (Pukhova et al., 2017).

The TFR was calculated in average for all epochs that corresponded to the same finger button press (or state), on the 5 Hz to 60 Hz frequency range. That includes the alpha, beta and gamma bands. Discrete frequencies at regular intervals of 3 Hz (5, 8, 11 Hz, and so on) were chosen.

# Characterization and Classification of Finger Movement-Related Brain Activity using Optically Pumped Magnetometers

For each of these frequencies, a specific number of cycles in our analysis was chosen, which was always half the frequency. For example, at 10 Hz, 5 cycles were used. This method helped us get a good balance between capturing the details of time changes and the details of frequency changes in the signal. The result was decimated by a factor of 3 in the time-domain to reduce memory usage – only after the frequency conversion was performed, preventing aliasing.

Plotting of the TFRs (1 plot per state) was done using *AverageTFR.plot()* method, setting the baseline to  $-2\text{ s}$  to  $-0.57\text{ s}$ – the reason for choosing this baseline is explained in Section 2.2.5)- and using the *logratio* mode. This mode applies a baseline correction that consists in dividing the data by the mean of the baseline values and taking logarithm of this ratio to provide the baseline-corrected value. This logarithm approach was employed since it compresses the dynamic range of the data and makes it easier to visualize and compare changes in power across different frequency bands.

## Synchronization Power Frequency

ERS occur normally within 1 s to 1.5 s after an event occurs, while ERDs occur within milliseconds (Pfurtscheller, 1992). In the TFR plots, a drop in power in the beta band was observed around time zero: the ERD. Following that drop, a surge in power in the beta band can be easily noted in the interval 0.75 s to 1.75 s, which corresponds with the ERS.

A variable portraying the frequency power profile during ERS was created: Synchronization Frequency Power (SFP). It was calculated using the same baseline correction as for TFR, and then for each frequency, the mean was taken for the interval (0.75 s to 1.75 s). That resulted in a single power value for each frequency, in each channel, for each finger. The mean across all fingers was also calculated to be used as reference.

## Beta Power over Time

Knowing that the beta band power is an important indicator for ERD and ERS events (Neuper et al., 2006), and after observing in the TFR some differences on the beta band before and after the event, the next step was looking at the fluctuations of beta-band power over time. It will be referred as Beta Power from now on.

The same power values from the TFR (with baseline correction) were taken, and then, the mean over the power of all the beta band frequencies (12.5 Hz to 30 Hz) was calculated. That was done for each time point, in each channel, for different fingers. The mean across all fingers was also calculated to be used as reference in plotting.

## Beta Power across all Sensors

In the previous two approaches (frequency and temporal-based), a very important aspect of OPM was being disregarded: the importance of how the Beta Power is distributed across sensors.

To look at the overall dynamics of power patterns across all sensors, the mean of the Beta Power was extracted at the intervals of highest importance for the study. Those were (-0.5 s to 0.5 s) - *Start*, ERD- and (0.75 s to 1.75 s)- *Synchronization*, as it was the interval in which the ERS were observed. That yielded two values for every channel per finger.

Since the sensors contained three channels (X, Y and Z), three different plots were produced (one per dimension). The plots illustrated the mean Beta Power at the *Start* of the epoch for each finger, and the patterns of the Beta Power while *Synchronization*.

### 2.3.5 Deep-Learning Approaches

Two Deep-Learning classifiers were used to see whether they could unveil the hidden differences within states. They were used for both two-class classifications (or binary), in which one state was compared to all others individually (Finger 1 vs. Finger 2, Finger 1 vs. Finger 3, ..., Finger 4 vs. Finger 5), and multi-class classifications, in which we compared all at the same time – thanks to a final layer with 5 classification outputs.

Both algorithms were performed using a 5-fold cross-validation paradigm to ensure the robustness of the results, and a 80/20 split between train and test data. Data used as input also was subtracted its mean and divided by its standard deviation to have a mean equal to zero and a variance of one, avoiding absolute changes to drive our classification, rather than relative ones.

#### DeepConvNet

Schirrmeister et al. (2017) developed **DeepConvNet**, a complex Convolutional Neural Network (CNN) with 4 convolutional pooling blocks, originally implemented for EEG signals classification. This network was selected for its specialization in classifying brain signals, addressing both spatial and temporal aspects, drawing inspiration from computer vision architectures. This is crucial when classifying time series data, and this network has demonstrated its effectiveness in classifying neural signals.

A diagram of the architecture can be found in 2.4. It consists of four sequential convolution-max-pooling blocks.

The first block is specially designed to handle EEG/MEG input, starting with a "temporal" convolution layer of 25 Linear Units, with a  $10 \times 1$  window. This layer is meant to apply filters across the time dimension to detect changes or patterns over time. A padding of 5 was set to manage the differences between input and output size. That is followed by a spatial filter spanning all channels using 25 Exponential Linear Units (ELUs). The purpose of this layer is learning complex spatial patterns and relationships among different brain regions. A max-pooling layer with a  $3 \times 1$  stride- reducing the dimensionality of the feature maps- and a 0.5 Dropout layer, preventing overfitting by randomly dropping 50% of the units, completed the first block.

The other 3 convolutional blocks share a common structure, having a  $10 \times k$  convolution layer with  $2k$  as the number of ELUs, and padding equals to 5. They gradually increase in size, with  $k = 25, 50$  and  $100$ . After each convolution layer, a max-pooling layer with

a  $3 \times 1$  stride and a 0.5 Dropout layer follows. The role of these 3 convolutional blocks is detecting hidden patterns in the data, capturing a wider range of features as the data progresses through the blocks.

Batch normalization was applied to the output of each convolutional layer before the non-linearity, stabilizing the learning process and reducing the number of training epochs to effectively train the network.

The network concludes with a fully connected (dense) layer of 200 units, which ultimately will learn complex mappings from the feature map to the classes. A *log softmax* function is applied to the output of each category, yielding the probabilities of assigning each epoch to a specific class.

A standard Adam optimizer was used to train the network, running 200 epochs with a learning rate of  $1 \times 10^{-3}$ . A longer training was not executed since overfitting started to appear after 200 epochs. All parameters used in the network were chosen because they were the optimal ones found in the original study.

## LF-CNN

**LF-CNN** (linear finite-impulse-response), a simpler CNN than DeepConvNet, was also originally implemented for a classification task involving MEG signals (Zubarev et al., 2019). This network was chosen for its simplicity compared to DeepConvNet. A network with a higher number of parameters is not always better at classifying due to over-fitting (Ying, 2019). LF-CNN, apart from being simpler than DeepConvNet, has also shown to be able to classify movement-related brain signals.

A diagram of the architecture can be found in 2.5. It starts with linear input layers called the spatial demixing layer, which are spatial filters themselves, like the ones in DeepConvNet. These spatial filters can be related to the spatial activation patterns of the latent sources, transforming the dimensions of the data from  $n$  channels to  $k$ . A temporal convolutional layer with a window of  $l \times 1$  dimensions follows. A non-linearity using Rectified Linear Units (ReLU) and a 0.5 Dropout layer was used after the spatio-temporal filters. Max pooling with a stride of  $2 \times 1$ , the flattening of the output, and a dense layer at the end with a *log softmax* function to calculate the probabilities of each category complete the network. The function of all layers within the network are explained in the DeepConvNet, since they share most building blocks.

In the spatial demixing layer,  $n = 32$  spatial filters were used, and  $l = 7$  was the length of the temporal filter. An Adam optimizer was used, running 200 epochs with a learning rate of  $3 \times 10^{-4}$ . All the parameters chosen were the optimal ones from the original paper.

*Characterization and Classification of Finger Movement-Related Brain Activity using Optically Pumped Magnetometers*

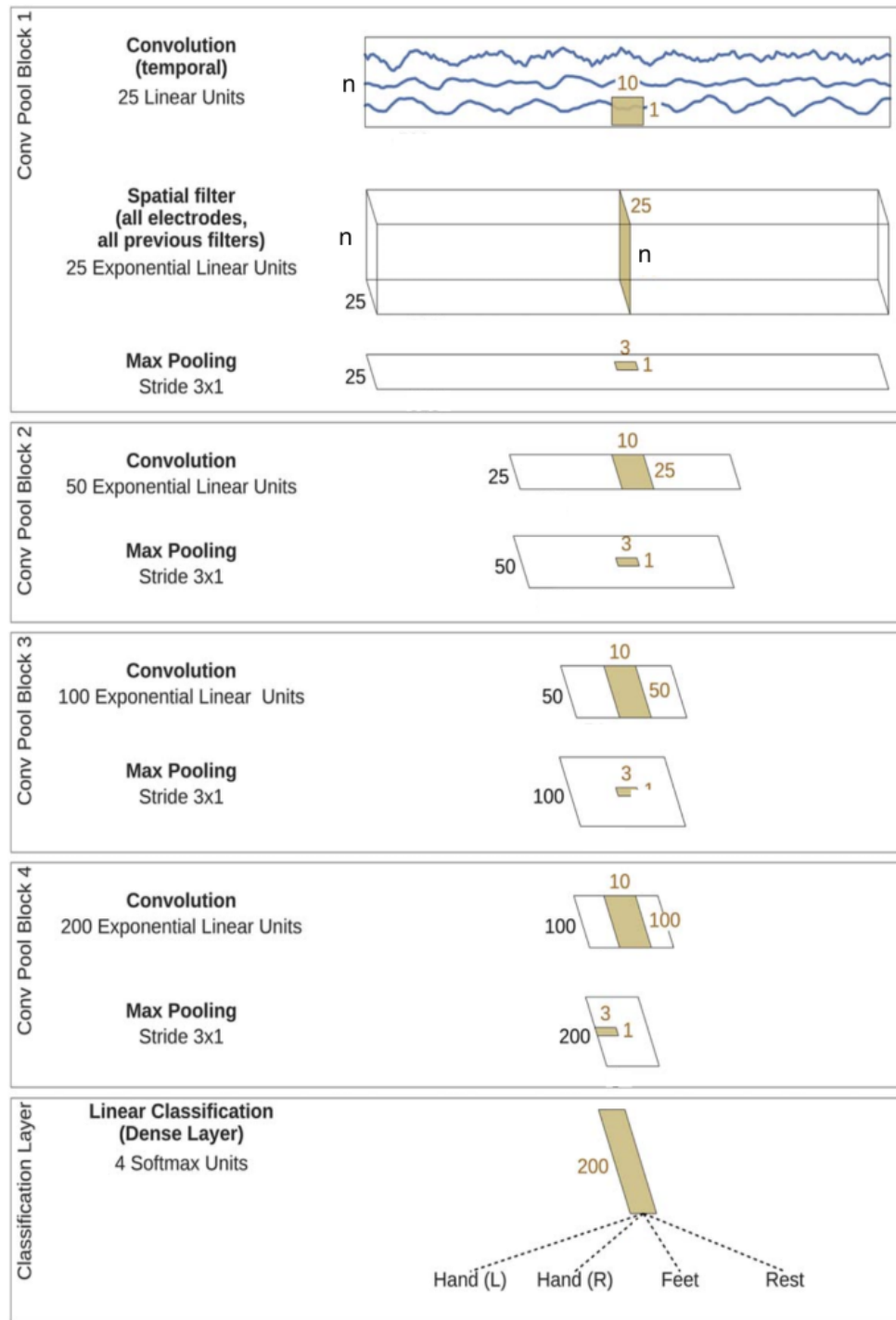


Figure 2.4: **DeepConvNet Architecture.** Diagram showing the different blocks that form the DeepConvNet architecture, formed by 5 convolutional pooling blocks and a classification layer at the end. The variable  $n$  corresponds to the number of channels of the raw data. Based on image extracted from Schirrmeister et al. (2017).

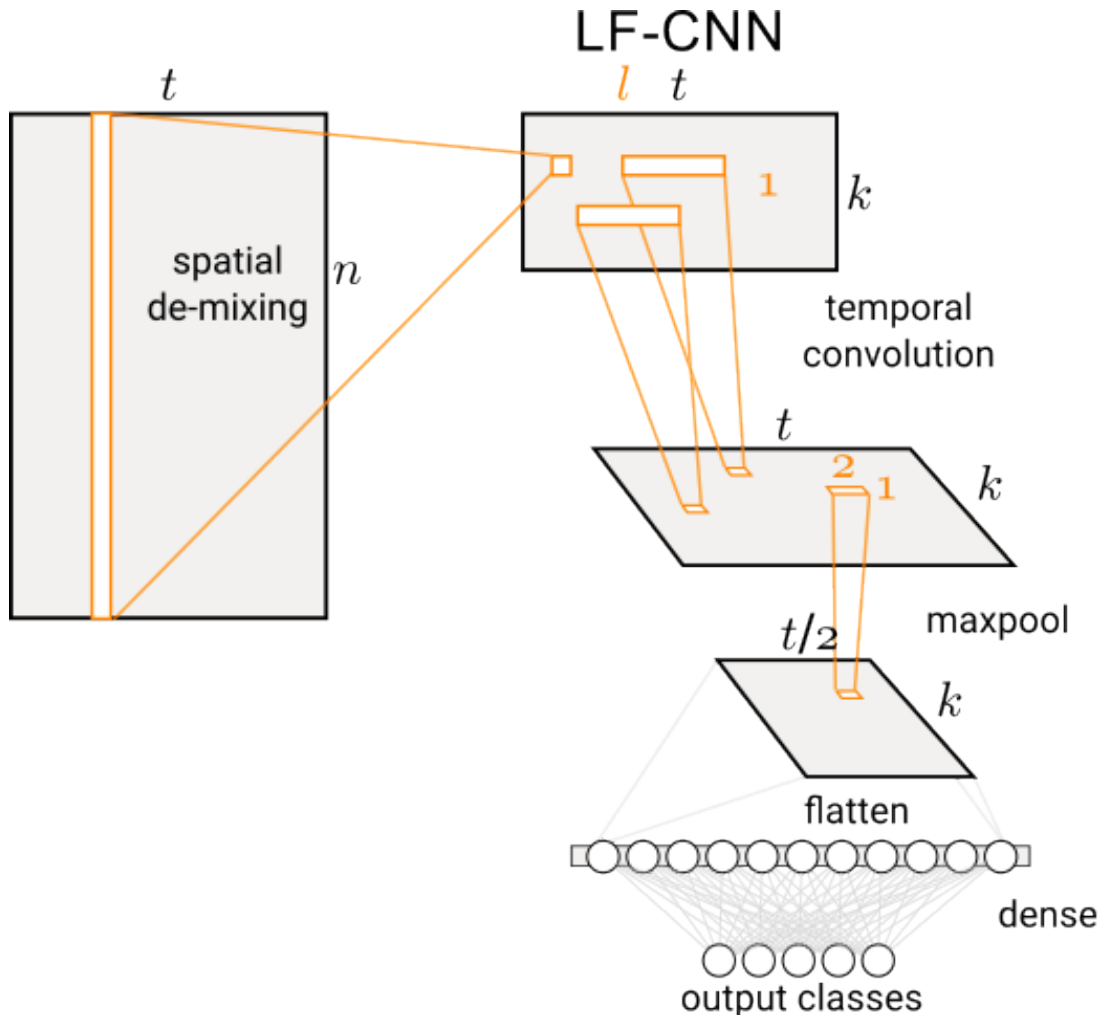


Figure 2.5: **LF-CNN Architecture.** Diagram showing the different layers that form the LF-CNN architecture. It starts with a spatial de-mixing layer, followed by a temporal convolution one, max-pooling, flattening and a dense layer. The variables  $t$ ,  $n$ ,  $k$ , and  $l$  stand for number of time steps, number of channels, number of spatial filters, and length of the temporal filter respectively. Based on image extracted from Zubarev et al. (2019).

*Characterization and Classification of Finger Movement-Related Brain Activity using  
Optically Pumped Magnetometers*

# 3 Results

## 3.1 Time-Frequency Representation

The TFRs allow us to look into how the frequency content of our epochs changes over time. As explained before, brain activity connected to the button presses is expected to be more apparent in the C3 area. Thus, the **C3 center channel** was used to represent these dynamics visually.

The TFR plots in Fig. 3.1 show how the power of each frequency fluctuates during an epoch- in average for each state. For all 5 states (fingers), a decrease in power around the time 0 s can be observed, which is the time of the button press; and a surge in power 1 s to 1.5 s after the button press.

There are noticeable variations in the dynamics across different states. The third finger, corresponding to the middle finger, exhibits a pronounced fluctuation over time, whereas the fifth finger shows a negligible increase in power. The second and fourth fingers demonstrate dynamics like the ones of the middle finger, although with reduced amplitudes; they are quite similar to each other in this regard. The first finger, while differing slightly from the second and fourth, also displays this pattern.

The plots corresponding to the TFR of the other channels, FW[X], HI[X], FY[Y] and HQ[Z] can be found in Section .2.

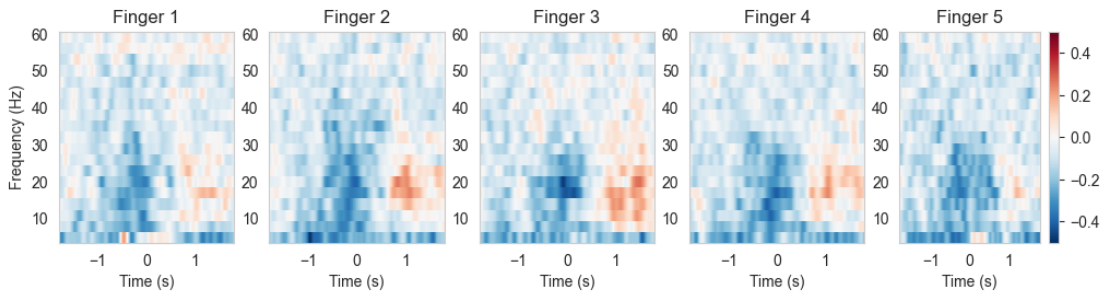


Figure 3.1: **Time Frequency Representation for different states.** Plots depicting the TFR of the center channel LQ[X]. The TFR is calculated in average across all epochs pertaining to the same state. Time equals zero represents the button press.

## 3.2 Synchronization Frequency Power

The SFP profiles for the five channels can be found in Fig. 3.2. From an overall overview, it can be seen that the curves of the C3 electrodes (X dimension channels: LQ[X], FW[X], and HI[X]) follow very similar dynamics. However, the FY[Y] and HQ[Z] channels show lower power in general for all frequencies. The most prominent frequencies for all of them lie within the beta range (12.5 Hz to 30 Hz) for all plots.

C3 channels show the biggest differences between states, specially in a significant peak appreciated in the (12.5 Hz to 20 Hz) range, with high differentiability between Finger 3 (green) and Finger 5 (purple). The other finger curves lie within them, close to the average SFP in black. In the case of FW[X], the Finger 3 vs Finger 5 difference is most significant, seeing that there is not even a surge in amplitude in the (12.5 Hz to 20 Hz) range for the Finger 5 state. All in all, C3 channels show similar profiles to each other. This finding contrasts with our initial hypothesis, which suggested that each channel might predominantly reflect a different button press or would show different patterns across states.

In the FY[Y] plot, this (12.5 Hz to 20 Hz) surge is also noted, but with lower contrast (also being the Fingers 3 vs 5 the most different states). In the HQ[Z] plot, a completely different profile arises, with little to no differentiation among channels. Finger 3 presented there also the highest amplitude, far away from the other profiles and average.

## 3.3 Beta Power over Time

The Beta Power profiles over time for the five channels can be found in Fig. 3.3, along with the variance of each state. The variance is a good indicator for the differences between ERD and ERS intervals.

Overall dynamics are very similar to the ones observed in SFP: it makes sense since it is the same data visualized differently. The LQ[X] channel shows the highest variance in Beta Power among the five of them. The ERD can be easily detected around time 0 s, and the ERS around 0.75 s to 1.75 s. That is why the latter was used as *Synchronization* interval for the SFP calculation. The other C3 channels show analogous dynamics to the LQ[X] channel but with negative power in general (showing only a ERD but not such a pronounced ERS).

In the C3 electrodes, similarly as for the SFP case, Finger 5 shows the lowest amplitude and variance, and Finger 3 shows the highest surge. The latter also shows a small bump at 1.5 s, being the only one in which that behaviour can be appreciated.

HQ[Z] shows a similar profile to the C3 electrodes although with a much lower amplitude and variance. FY[Y] shows no change from the baseline: the Beta Power is almost constant throughout the whole epoch.

# Characterization and Classification of Finger Movement-Related Brain Activity using Optically Pumped Magnetometers

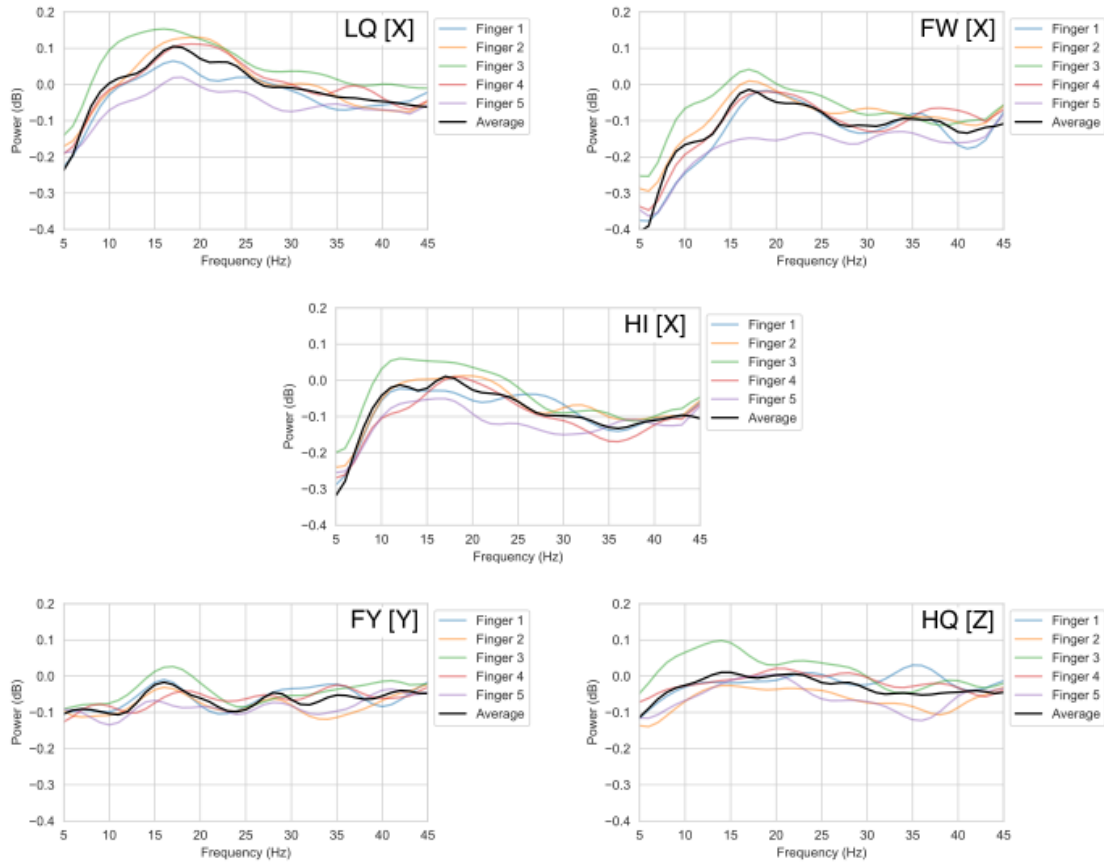


Figure 3.2: **SFP for 5 different channels.** Plots depicting the Synchronization Frequency Power profiles of different states in 5 different channels: LQ[X], FW[X], HI[X], FY[Y], and HQ[Z]. In lower opacity, the SFP of all fingers, and in higher opacity, in black, the average of all of them.

## 3.4 Beta Power across all Sensors

The target of this approach was looking at the differences in Beta Power across all sensors and if the overall patterns change among states. This can be observed in Fig. 3.4.

The results in all axes show a greater Beta Power at the *Synchronization* interval than in the *Start* one, as expected. Given the direction of the magnetic fields and the orientation of each sensor, some sensors exhibit a higher amplitude of signal (and therefore power) only for a specific dimension. That is why it is important looking at all dimensions separately.

In dimension X, the sensors in the C3 area—area of upmost interest for this study—present a higher power, and there is a patch with higher power in the Finger 3 compared to the others. Apart from that, overall dynamics remain similar. In the Y and Z axes all states look almost identical, making discrimination a very hard task.

# Characterization and Classification of Finger Movement-Related Brain Activity using Optically Pumped Magnetometers

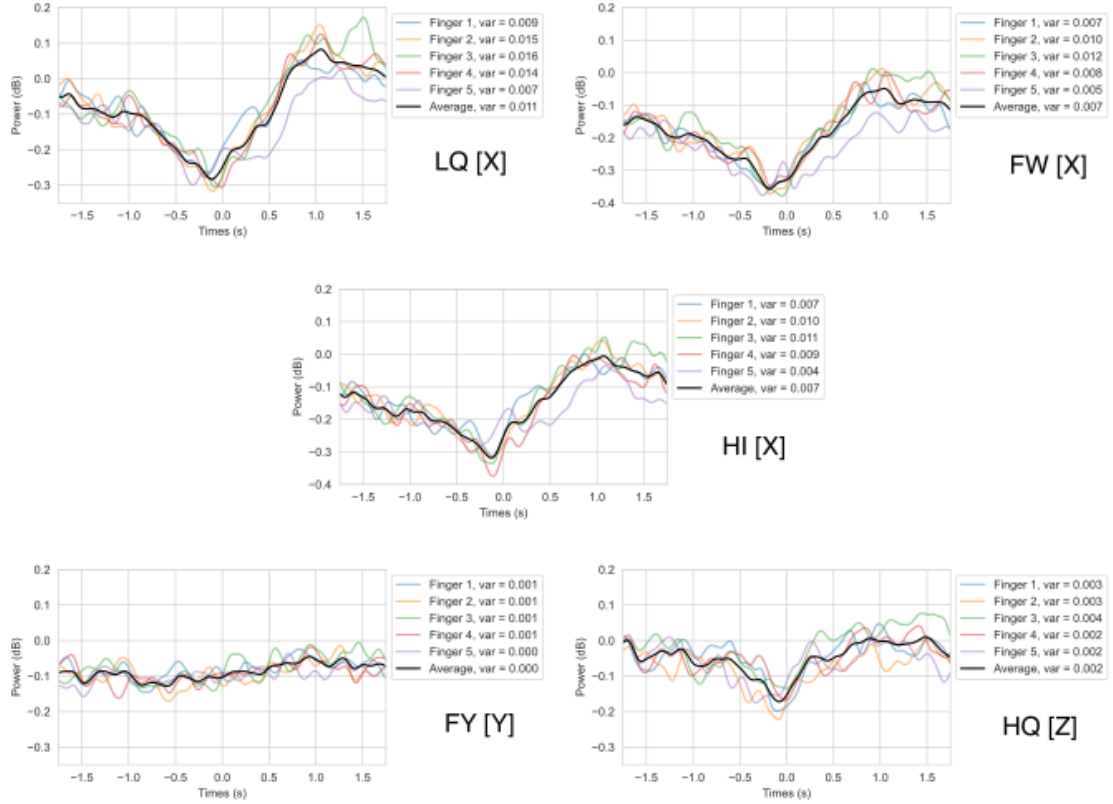


Figure 3.3: **Beta Power over time.** Plots depicting the Beta Power over time for 5 different channels: LQ[X], FW[X], HI[X], FY[Y], and HQ[Z]. In lower opacity, the Beta Power of all fingers and in higher opacity, in black, the average of all of them. Time equals zero represents the button press. In the legend corresponding to each channel, the variance of the Beta Power of each state can be found.

## 3.5 CSP on Beta-Band

Sometimes the patterns defining the differences between states are not appreciated with the naked eye. That is where spatial filtering like CSP comes into play. Using CSP on the beta-band band-passed signal, binary classification on all comparisons of fingers was performed. None of the binary classification comparisons were successful. As it can be seen in Table 3.1, all of the classifications show an accuracy lower than 60 %. The one with highest eigenvalues (higher differentiability) and accuracy was the comparison between Finger 3 vs Finger 5, which is the one shown in Fig. 3.5.

In the visual representation of the X axis, it is notable that the area around the LQ[X] sensor, which was anticipated to have a significant impact on classification, indeed exhibits a very high absolute weight on the filter coefficients (around -0.6). This observation suggests that coefficients with high absolute values in both directions (negative and pos-

itive) play a crucial role in the classification process.

Nevertheless, all in all, patterns appear quite random across the brain for all axes. Coupling this observation with the detail that the eigenvalues are closely approximating 0.5, it can be deduced that the Common Spatial Patterns (CSP) algorithm was unsuccessful in identifying sufficiently discriminative spatial filters to differentiate between classes.

### 3.6 Finger Discrimination Classification

Since no clear distinction could be extracted from the visual representation of the states, more complex analyses were needed to look at the discriminability of the data.

Firstly, a more established method like the combination of CSP and LDA was used-explained before in Section 2.3.2. As observed in Fig. 3.1, the range of frequencies with higher amplitude and fluctuations lies within the beta range (12.5 Hz to 30 Hz). Thus, a band-passed filter on the beta frequencies was applied to the raw signal, and CSP was applied on the filtered output. Using LDA on the features extracted from it, binary classifications on finger-to-finger comparisons were performed.

Secondly, DeepConvNet and LF-CNN deep learning algorithms were used and the results came back overall with negative results. That means that, in general, no clear distinction was found between states. In the case of the multi-class classification problem (5 states), the DeepConvNet algorithm got a mean accuracy and standard deviation of  $21.7 \pm 3.9\%$ , while the LF-CNN got an accuracy of  $31.9 \pm 6.0\%$  (mean and standard deviation over 5 cross-validation). 20% represented chance level.

All **binary-classifications** (finger vs. finger) can be observed in Table 3.1. There, only the comparison between Finger 1 and 5 (thumb and little finger) shows a classification accuracy over 70 % in the case of LF-CNN. In the Discussion, it will be addressed why this minimum of 70 % is important, and its relationship to the state-of-the-art results.

Comparison	CSP-LDA Beta Band	DeepConvNet	LF-CNN
Finger 1 vs 2	$47.1 \pm 7.5$	$53.8 \pm 8.3$	$58.4 \pm 11.2$
Finger 1 vs 3	$39.4 \pm 7.2$	$56.7 \pm 7.5$	$63.2 \pm 6.0$
Finger 1 vs 4	$41.9 \pm 6.6$	$56.0 \pm 1.6$	$58.6 \pm 3.2$
Finger 1 vs 5	$48.1 \pm 5.9$	$59.0 \pm 0.9$	$76.3 \pm 3.6$
Finger 2 vs 3	$52.3 \pm 5.2$	$56.9 \pm 5.8$	$51.0 \pm 4.7$
Finger 2 vs 4	$49.0 \pm 5.2$	$54.8 \pm 6.0$	$50.3 \pm 7.2$
Finger 2 vs 5	$49.0 \pm 5.6$	$56.5 \pm 2.0$	$65.6 \pm 6.3$
Finger 3 vs 4	$51.2 \pm 6.0$	$51.3 \pm 5.0$	$48.1 \pm 9.1$
Finger 3 vs 5	$56.8 \pm 6.4$	$52.9 \pm 6.1$	$63.9 \pm 5.2$
Finger 4 vs 5	$50.0 \pm 6.6$	$49.1 \pm 9.2$	$54.8 \pm 4.4$
<b>Average</b>	$48.5 \pm 5.4$	$54.7 \pm 6.5$	$59.0 \pm 10.4$

Table 3.1: **Binary classification accuracy results.** Average accuracy percentages for DeepConvNet, LF-CNN, and LDA classifications using CSP features within the beta band, along with their respective standard deviations, across all state comparisons. The comparison between Finger 1 and Finger 5 with LF-CNN shows the highest accuracy.

Characterization and Classification of Finger Movement-Related Brain Activity using  
Optically Pumped Magnetometers

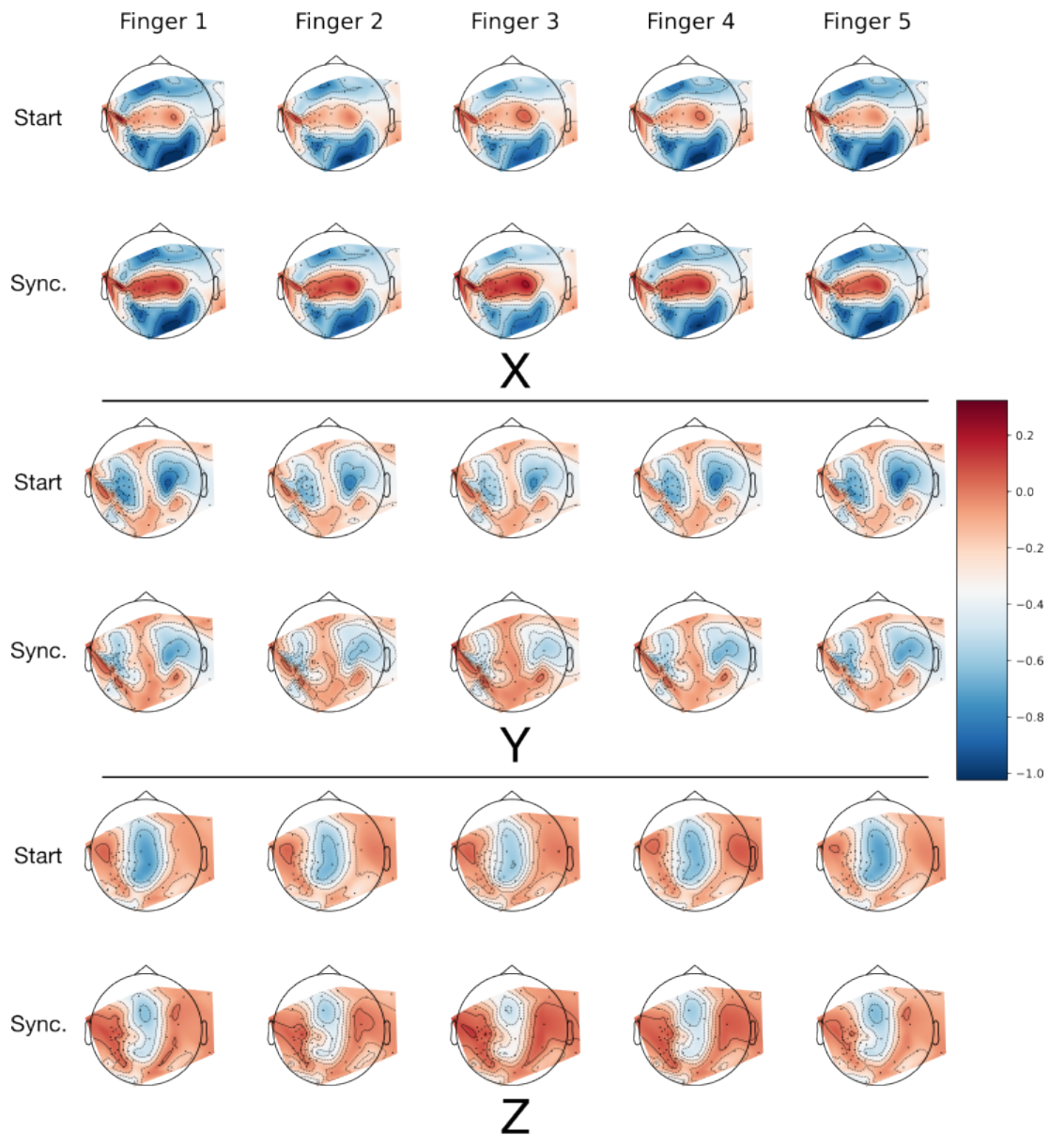


Figure 3.4: **Beta Power across all sensors.** Beta Power at the *Start* interval (-0.5 s to 0.5 s) and the *Synchronization* interval (0.75 s to 1.75 s) for all different states. Dimensions X, Y, and Z are plotted separately. The scale of the power is represented in dB.

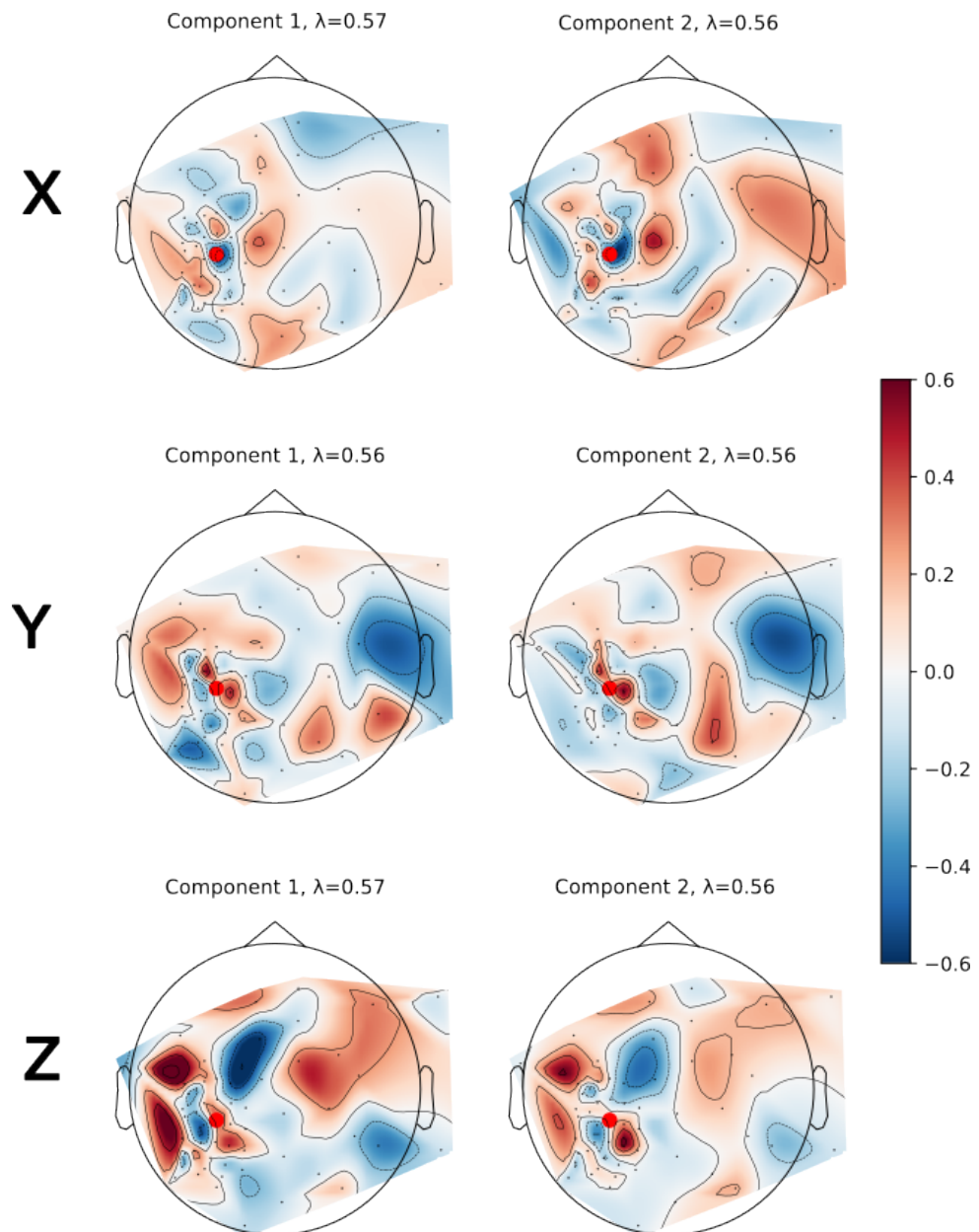


Figure 3.5: **CSP on beta band. Finger 3 vs Finger 5 comparison.** Spatial patterns of the CSP when performed separately on X, Y, and Z magnetic directions. The eigenvalue to each spatial filter appears on top of each plot. The red dot indicates the position of the LQ sensor.

## 4 Discussion

In this study, a varied set of state-of-the-art approaches to analyse and classify data were used. Those approaches ranged from frequency-based to time-based approaches, including standardized signal decomposition and novel deep-learning algorithms. The sole purpose of these efforts was to determine if OPM signals could outperform the existing techniques currently utilized in brain-computer interfaces (BCIs).

The initial TFR plots provided some crucial insight, showing visual differentiability among states for the channel located on the brain area that should be the most relevant for this task: C3. The decrease in power in Fig. 3.1 around time 0 s is what would be expected: the coupling of an event and the desynchronization of the area controlling it (ERD). Also, the surge in power in the 0.75 s to 1.75 s interval showed a great indicator of an ERS also happening.

The appearance of both events could indicate that the data was successfully portraying a direct response in brain activity to the button presses the participant was performing. The observation of differences in the brain activity between states encouraged us to engage in a more in-depth analysis.

For that reason, SFP plots were devised. They provided a way to look at the frequency profiles on ERS for different finger taps and were the first analysis tool: looking at the profiles for different channels and seeing whether they were different enough to run multi-class classification.

In the SFP plot in Fig. 3.2, C3 channels (LQ[X], FW[X], and HI[X]) showed a big difference in the power of the (12.5 Hz to 20 Hz) band between Finger 3 and 5. This hinted towards the possibility of differentiating them in a binary classification paradigm. It also showed that each state might have its own SFP profile. However since the 5 classes shared such a similar profile, it gave us no room for multi-class classification.

It provided a clear insight though: if any differences were to exist, they would lie within the beta band range (12.5 Hz to 30 Hz), as that is where the main differences in the plot can be found. Beta band is already known to be key for ERS/ERD modulation, so these findings looked to be pointing in the right direction (Neuper et al., 2006).

Nevertheless, the problem with SFP plots is that they disregard the temporal component of our data, as it only looks at the ERS interval. Seeing that the beta band is the key frequency among all of them, the Frequency dimension was sidelined and the focus shifted towards the temporal dimension. That is why the Beta Power over time plots were introduced, where the mean in the frequency domain over the beta-band was taken (Fig. 3.3). In these plots, it can be seen that there are two very distinct regimes: the ERD at time 0 s and the ERS at the 0.75 s to 1.75 s interval.

These charts also suggest that multi-class classification might be difficult because the differences between states are too small. Binary classification was still a possibility, since

differences can be seen between the Finger 3 and Finger 5 profiles.

These previous approaches were also devised to investigate whether the SFP or the Beta Power over time differed between neighboring sensors in the C3. That would be the base for successful finger discrimination: each finger activating a different part of the brain. That would yield a good basis for finger discrimination across sensors. However, in both figures, the profiles of all adjacent sensors looked very similar from one another: Finger 3 showed always the highest amplitude while Finger 5 shows always the lowest one.

In these two approaches (frequency and temporal-based), a very important aspect of OPM was being disregarded though: the high number of channels available in OPM helmets.

For that reason, Beta Power was plotted across all sensors at the key intervals described before: (-0.5 s to 0.5 s)- ERD- and (0.75 s to 1.75 s)- ERS; collapsing the data over both time and frequency axes. In Fig. 3.4, an increase in Beta Power can be overall observed in all dimensions and channels from the *Start* interval to the *Synchronization* interval. The intrinsic orientation of the sensors with respect to the brain magnetic fields create those patterns in dimensions X, Y and Z.

In the X axis plot, a difference in amplitude can again be observed between the Finger 3 and Finger 5. However, the general differences between states do not appear to be enough to perform any multi-class assessment.

Using spatial filters (CSP) on the beta band also did not reveal any clear patterns in the brain that could help with accurate classification; the results seemed almost random. The LQ[X] channel appeared to hold some significance for classification given the absolute value of the spatial patterns in its area (Fig. 3.5). That shows that it was right to focus the study on that area, even though the differences are too subtle to perform any classification. Also, the eigenvalues remain close to 0.5, which represented almost chance level. We only plotted the comparison between Finger 3 and Finger 5, since no other comparison showed better eigenvalues or classification accuracy.

All these previous approaches primarily relied on visualizations, requiring differences to be discerned solely through plots. However, in neural signal classification, these distinctions tend to be subtle, necessitating the use of more sophisticated classification methods.

All multi-class classification attempts with LF-CNN and DeepConvNet remained too close to a random 20% accuracy. The results of binary comparisons can be appreciated in Table 3.1. There, almost all values remained close to 50% (chance level), although the Finger 1 vs Finger 5 comparison rose to show a result that comes close to the state-of-the-art classification standard: 76% using the LF-CNN versus the 77% reported in EEG in Liao et al. (2014). The traditional CSP-LDA paradigm showed completely chance level results for binary classification.

The LF-CNN demonstrates the highest overall classification accuracy and variability among the tested methods. However, despite obtaining positive results for the comparison between Finger 1 to Finger 5, the mean accuracy across all comparisons remains too close to 50% to be considered a significant advance over existing techniques.

*Characterization and Classification of Finger Movement-Related Brain Activity using  
Optically Pumped Magnetometers*

This study has indicated that classification using OPM data might be possible, though it may not yet match the effectiveness of other established techniques, particularly invasive recordings. Additionally, exploring other classification methods, such as deep learning approaches with different architectures, could be a worthwhile pursuit. The representations we have found for the brain activity corresponding to each finger movement is too close to one another to be differentiated. Seedat et al. (2023) showed that simultaneous whole-head electrophysiological recordings using both EEG and OPM can be performed, and combining features from both EEG and OPM could improve drastically the classification of brain signals into a working BCI with finger discrimination.

Even if this study would have come out with more conclusive results, these would still have one big constraint: classification is performed offline. That means, no actual feedback control can be relayed into BCI-controlled hardware. In the case more positive results would have been drawn from this study, these approaches should be used to find informative features that could be applied in an online matter.

As in Mondini et al. (2016), EEG-controlled BCI normally relies on thresholds to be activated. That is, setting a boundary for amplitude of the signal itself or the power of a frequency within that signal. In the case of finger movement discrimination, the idea would be setting different thresholds in different channels and creating a set of thresholds that would activate each finger differently. With this study, the right combination of channels could have been found. To find which channels were informative and how, this preliminary study was certainly needed.

*Characterization and Classification of Finger Movement-Related Brain Activity using  
Optically Pumped Magnetometers*

## 5 Limitations

Throughout the analysis of the results and the conception of the study, various limitations on it were identified. To start with, a control recording was not acquired. That probably is the main limitation of the whole study.

A control recording, where cues to move each finger were presented but no button was pressed nor any movement was imagined, was missing. Given that movement imagery closely mirrors the changes in brain activity of actual movement and is essential for BCI, it is crucial to exclude both movement and movement imagery from control recordings (Jeon et al., 2011).

This control recording would have yielded a standard to which the ERFs could be compared. Only a series of resting recordings was acquired for analyzing differences in overall power spectra. However, since these recordings lacked cues, epoching was randomly assigned. Consequently, epochs could not be utilized in a classification paradigm aimed at distinguishing between movement and resting epochs.

Another limitation of the study is the inclusion of only one participant in it. If more participants had been included, we might have observed a different outcome in the results. One of the biggest research challenges for BCIs is the problem of "BCI incompetence". BCI control is not possible work for a non-negligible portion of users (estimated 15 to 30%) (Blankertz et al., 2009). This participant may not have demonstrated the hypothesized activity, but it is possible that others might have exhibited it. On the other hand, if more participants had taken part in the study and showed no significant differences between finger taps, the results would have been more conclusive.

*Characterization and Classification of Finger Movement-Related Brain Activity using  
Optically Pumped Magnetometers*

## 6 Conclusion and Next Steps

Discriminating finger movements on a neural level is a very complex task. Efforts towards its development continue to grow as tools, hardware and software improve.

The results with invasive recordings yield the most promising results but it is difficult nowadays to show that the advantages of invasive BCIs outweigh all possible complications coming with them. The non-invasive standard, EEG, lacks spatial resolution and electrodes located in close locations tend to share too much information due to volume conduction. MEG, and in particular, OPM-MEG tackles this issue.

This study's hypothesis was based on the idea that higher spatial resolution would reveal distinct activity in the C3 area channels, detectable by OPMs. It was anticipated that different fingers would generate unique activity patterns across sensors, allowing for the establishment of precise thresholds for key channels, enhancing BCI control.

With the analysis performed in our participant, we achieved results close to the state-of-the-art in offline binary classification for one comparison (Finger 1 vs Finger 5). That shows the potential of OPMs for detecting ERF, ERD and eventually being a candidate for BCI control. However, as this positive result was not shared across all finger comparisons, the spatial resolution provided by the OPMs seems to be still insufficient for successful finger movement decoding.

Furthermore, we could see that choosing the right deep learning architecture is a crucial step that can lead to better outcomes in understanding and interpreting brain activity. For future research, combining EEG and OPM data could be beneficial for developing a more successful classification paradigm. Uniting features extracted from both OPM and EEG could significantly enhance the classification process.

All in all, this thesis delves into the potential of OPM technology in decoding fine-movement brain activity. Our research points towards an exciting future for OPM in BCI, and how its combination with new computation techniques, like deep-learning, will expand the field of BCI control.



# Bibliography

- Abiri, R., Borhani, S., Sellers, E. W., Jiang, Y., & Zhao, X. (2019). A comprehensive review of eeg-based brain–computer interface paradigms. *Journal of neural engineering*, 16(1), 011001.
- Allred, J., Lyman, R., Kornack, T., & Romalis, M. V. (2002). High-sensitivity atomic magnetometer unaffected by spin-exchange relaxation. *Physical review letters*, 89(13), 130801.
- Benesch, C., & Holloway, R. G. (1998). Economic impact of stroke and implications for interventions. *CNS drugs*, 9(Suppl 1), 29–39.
- Blankertz, B., Sanelli, C., Halder, S., Hammer, E., Kübler, A., Müller, K.-R., Curio, G., & Dickhaus, T. (2009). Predicting bci performance to study bci illiteracy. *BMC Neurosci*, 10(Suppl 1), P84.
- Boto, E., Bowtell, R., Krüger, P., Fromhold, M., Morris, P., Meyer, S., Barnes, G., & Brookes, M. (2016). The benefits of atomic magnetometers for meg: A simulation study. *PLoS ONE* doi, 10.
- Boto, E., Meyer, S. S., Shah, V., Alem, O., Knappe, S., Kruger, P., Fromhold, T. M., Lim, M., Glover, P. M., Morris, P. G., et al. (2017). A new generation of magnetoencephalography: Room temperature measurements using optically-pumped magnetometers. *NeuroImage*, 149, 404–414.
- Boto, E., Holmes, N., Leggett, J., Roberts, G., Shah, V., Meyer, S. S., Muñoz, L. D., Mullinger, K. J., Tierney, T. M., Bestmann, S., et al. (2018). Moving magnetoencephalography towards real-world applications with a wearable system. *Nature*, 555(7698), 657–661.
- Brookes, M. J., Leggett, J., Rea, M., Hill, R. M., Holmes, N., Boto, E., & Bowtell, R. (2022). Magnetoencephalography with optically pumped magnetometers (opm-meg): The next generation of functional neuroimaging. *Trends in Neurosciences*.
- Bu, Y., Harrington, D. L., Lee, R. R., Shen, Q., Angeles-Quinto, A., Ji, Z., Hansen, H., Hernandez-Lucas, J., Baumgartner, J., Song, T., et al. (2023). Magnetoencephalogram-based brain–computer interface for hand-gesture decoding using deep learning. *Cerebral Cortex*, bhad173.
- Cobb, W., London, G. B., Gastaut, H., Hess Jr, R., Jung, R., Magnus, O., et al. (1958). Report of the committee on methods of clinical examination in electroencephalography. *Electroencephalogr. Clin. Neurophysiol*, 10(2), 370–375.
- Current designs button boxes*. (2024). Retrieved February 6, 2024, from <https://www.curdes.com/mainforp/respondeddevices/buttonboxes/hhsc-2x4-c.html>
- Fedorov, N., Shevtsov, O., & Ossadtchi, A. (2021). Motor-imagery bci with low-count of optically pumped magnetometers. *2021 Third International Conference Neurotechnologies and Neurointerfaces (CNN)*, 16–18.

*Characterization and Classification of Finger Movement-Related Brain Activity using Optically Pumped Magnetometers*

- Graimann, B., Townsend, G., Huggins, J., Schlägl, A., Levine, S., & Pfurtscheller, G. (2005). A comparison between using ecog and eeg for direct brain communication. *Proceedings of the EMBC05*.
- Handley, A., Medcalf, P., Hellier, K., & Dutta, D. (2009). Movement disorders after stroke. *Age and ageing*, 38(3), 260–266.
- Hari, R., & Salmelin, R. (2012). Magnetoencephalography: From squids to neuroscience: Neuroimage 20th anniversary special edition. *Neuroimage*, 61(2), 386–396.
- Hnazaee, M. F., Verwoert, M., Freudenburg, Z. V., van der Salm, S. M., Aarnoutse, E. J., Leinders, S., Van Hulle, M. M., Ramsey, N. F., & Vansteensel, M. J. (2022). Towards predicting ecog-bci performance: Assessing the potential of scalp-eeg. *Journal of Neural Engineering*, 19(4), 046045.
- Hussain, N., Alt Murphy, M., & Sunnerhagen, K. S. (2018). Upper limb kinematics in stroke and healthy controls using target-to-target task in virtual reality. *Frontiers in neurology*, 9, 300.
- Iivanainen, J., Stenroos, M., & Parkkonen, L. (2017). Measuring meg closer to the brain: Performance of on-scalp sensor arrays. *NeuroImage*, 147, 542–553.
- Impact of stroke* [World stroke organization]. (2024). Retrieved January 25, 2024, from <https://www.world-stroke.org/world-stroke-day-campaign/about-stroke/impact-of-stroke>
- Jeon, Y., Nam, C. S., Kim, Y.-J., & Whang, M. C. (2011). Event-related (de) synchronization (erd/ers) during motor imagery tasks: Implications for brain-computer interfaces. *International Journal of Industrial Ergonomics*, 41(5), 428–436.
- Jia, X., & Kohn, A. (2011). Gamma rhythms in the brain. *PLoS biology*, 9(4), e1001045.
- Kastler, A. (1951). Méthodes optiques d'étude de la résonance magnétique. *Physica*, 17(3-4), 191–204.
- Kim, Y. W. (2022). Update on stroke rehabilitation in motor impairment. *Brain & Neurorehabilitation*, 15(2).
- Liao, K., Xiao, R., Gonzalez, J., & Ding, L. (2014). Decoding individual finger movements from one hand using human eeg signals. *PloS one*, 9(1), e85192.
- Light, G. A., Williams, L. E., Minow, F., Sprock, J., Rissling, A., Sharp, R., Swerdlow, N. R., & Braff, D. L. (2010). Electroencephalography (eeg) and event-related potentials (erps) with human participants. *Current protocols in neuroscience*, 52(1), 6–25.
- Lin, P. T., Sharma, K., Holroyd, T., Battapady, H., Fei, D.-Y., Bai, O., & Signorelli, F. (2013). A high performance meg based bci using single trial detection of human movement intention. *Functional brain mapping and the endeavor to understand the working brain*, 17–36.
- Lotte, F., & Guan, C. (2010). Regularizing common spatial patterns to improve bci designs: Unified theory and new algorithms. *IEEE Transactions on biomedical Engineering*, 58(2), 355–362.
- Mane, R., Chouhan, T., & Guan, C. (2020). Bci for stroke rehabilitation: Motor and beyond. *Journal of neural engineering*, 17(4), 041001.

*Characterization and Classification of Finger Movement-Related Brain Activity using  
Optically Pumped Magnetometers*

- Mellinger, J., Schalk, G., Braun, C., Preissl, H., Rosenstiel, W., Birbaumer, N., & Kübler, A. (2007). An meg-based brain–computer interface (bci). *Neuroimage*, 36(3), 581–593.
- Meng, Y., Zhang, D., Hai, H., Zhao, Y.-Y., & Ma, Y.-W. (2020). Efficacy of coupling intermittent theta-burst stimulation and 1 hz repetitive transcranial magnetic stimulation to enhance upper limb motor recovery in subacute stroke patients: A randomized controlled trial. *Restorative neurology and neuroscience*, 38(1), 109–118.
- Mondini, V., Mangia, A. L., Cappello, A., et al. (2016). Eeg-based bci system using adaptive features extraction and classification procedures. *Computational intelligence and neuroscience*, 2016.
- Nann, M., Cordella, F., Trigili, E., Lauretti, C., Bravi, M., Miccinilli, S., Catalan, J. M., Badesa, F. J., Crea, S., Bressi, F., Garcia-Arancil, N., Vitiello, N., Zollo, L., & Soekadar, S. R. (2021). Restoring activities of daily living using an eeg/eog-controlled semiautonomous and mobile whole-arm exoskeleton in chronic stroke. *IEEE Systems Journal*, 15(2), 2314–2321.
- Neuper, C., Wörz, M., & Pfurtscheller, G. (2006). Erd/ers patterns reflecting sensorimotor activation and deactivation. *Progress in brain research*, 159, 211–222.
- Nicolas-Alonso, L. F., & Gomez-Gil, J. (2012). Brain computer interfaces, a review. *sensors*, 12(2), 1211–1279.
- Optically pumped magnetometers from quspin guide drones & brain imaging*. (2024). Retrieved February 6, 2024, from <https://magneticsmag.com/optically-pumped-magnetometers-from-quspin-guide-drones-brain-imaging/>
- Ordikhani-Seyedlar, M., Lebedev, M. A., Sorensen, H. B., & Puthusserypady, S. (2016). Neurofeedback therapy for enhancing visual attention: State-of-the-art and challenges. *Frontiers in neuroscience*, 10, 205322.
- Paek, A. Y., Kilicarslan, A., Korenko, B., Gerginov, V., Knappe, S., & Contreras-Vidal, J. L. (2020). Towards a portable magnetoencephalography based brain computer interface with optically-pumped magnetometers. *2020 42nd Annual International Conference of the IEEE Engineering in Medicine & Biology Society (EMBC)*, 3420–3423.
- Pedersen, M., Abbott, D. F., & Jackson, G. D. (2022). Wearable opm-meg: A changing landscape for epilepsy. *Epilepsia*, 63(11), 2745–2753.
- Pfurtscheller, G. (1992). Event-related synchronization (ers): An electrophysiological correlate of cortical areas at rest. *Electroencephalography and clinical neurophysiology*, 83(1), 62–69.
- Pfurtscheller, G., & Da Silva, F. L. (1999). Event-related eeg/meg synchronization and desynchronization: Basic principles. *Clinical neurophysiology*, 110(11), 1842–1857.
- Prabhakaran, S., Ruff, I., & Bernstein, R. A. (2015). Acute stroke intervention: A systematic review. *Jama*, 313(14), 1451–1462.
- Prochazka, A., Kukal, J., & Vysata, O. (2008). Wavelet transform use for feature extraction and eeg signal segments classification. *2008 3rd International symposium on communications, control and signal processing*, 719–722.

*Characterization and Classification of Finger Movement-Related Brain Activity using Optically Pumped Magnetometers*

- Pukhova, V., Gorelova, E., Ferrini, G., & Burnasheva, S. (2017). Time-frequency representation of signals by wavelet transform. *2017 IEEE Conference of Russian Young Researchers in Electrical and Electronic Engineering (EICConRus)*, 715–718.
- Quandt, F., Reichert, C., Hinrichs, H., Heinze, H.-J., Knight, R. T., & Rieger, J. W. (2012). Single trial discrimination of individual finger movements on one hand: A combined meg and eeg study. *NeuroImage*, 59(4), 3316–3324.
- Qzfm dimensions*. (2024). Retrieved February 6, 2024, from <http://quspin.com/products-qzfm/qzfm-dimensions/>
- Salmelin, R., Hámááláinen, M., Kajola, M., & Hari, R. (1995). Functional segregation of movement-related rhythmic activity in the human brain. *Neuroimage*, 2(4), 237–243.
- Schalk, G., & Leuthardt, E. C. (2011). Brain-computer interfaces using electrocorticographic signals. *IEEE reviews in biomedical engineering*, 4, 140–154.
- Schirrmeister, R. T., Springenberg, J. T., Fiederer, L. D. J., Glasstetter, M., Eggensperger, K., Tangermann, M., Hutter, F., Burgard, W., & Ball, T. (2017). Deep learning with convolutional neural networks for eeg decoding and visualization. *Human brain mapping*, 38(11), 5391–5420.
- Seedat, Z. A., Pier, K. S., Holmes, N., Rea, M., Al-Hilaly, L., Tierney, T. M., Pardington, R., Mullinger, K. J., Cross, J. H., Boto, E., et al. (2023). Simultaneous whole-head electrophysiological recordings using eeg and opm-meg. *medRxiv*, 2023–10.
- Seymour, R. A., Alexander, N., Mellor, S., O'Neill, G. C., Tierney, T. M., Barnes, G. R., & Maguire, E. A. (2022). Interference suppression techniques for opm-based meg: Opportunities and challenges. *NeuroImage*, 247, 118834.
- Shin, H.-C., Aggarwal, V., Acharya, S., Schieber, M. H., & Thakor, N. V. (2009). Neural decoding of finger movements using skellam-based maximum-likelihood decoding. *IEEE Transactions on Biomedical Engineering*, 57(3), 754–760.
- Singh, S. P. (2014). Magnetoencephalography: Basic principles. *Annals of Indian Academy of Neurology*, 17(Suppl 1), S107.
- Soekadar, S., Witkowski, M., Gómez, C., Opisso, E., Medina, J., Cortese, M., Cempini, M., Carrozza, M., Cohen, L., Birbaumer, N., et al. (2016). Hybrid eeg/eog-based brain/neural hand exoskeleton restores fully independent daily living activities after quadriplegia. *Science Robotics*, 1(1), eaag3296.
- Soekadar, S. R., Birbaumer, N., Slutsky, M. W., & Cohen, L. G. (2015). Brain-machine interfaces in neurorehabilitation of stroke. *Neurobiology of disease*, 83, 172–179.
- Stockley, R. C., Jarvis, K., Boland, P., & Clegg, A. J. (2021). Systematic review and meta-analysis of the effectiveness of mental practice for the upper limb after stroke: Imagined or real benefit? *Archives of Physical Medicine and Rehabilitation*, 102(5), 1011–1027.
- Toro, C., Deuschl, G., Thatcher, R., Sato, S., Kufta, C., & Hallett, M. (1994). Event-related desynchronization and movement-related cortical potentials on the ecog and eeg. *Electroencephalography and Clinical Neurophysiology/Evoked Potentials Section*, 93(5), 380–389.

*Characterization and Classification of Finger Movement-Related Brain Activity using  
Optically Pumped Magnetometers*

- Ulloa, J. L. (2022). The control of movements via motor gamma oscillations. *Frontiers in human neuroscience*, 15, 787157.
- Ushiba, J., & Soekadar, S. (2016). Brain-machine interfaces for rehabilitation of post-stroke hemiplegia. *Progress in brain research*, 228, 163–183.
- Vaid, S., Singh, P., & Kaur, C. (2015). Eeg signal analysis for bci interface: A review. *2015 fifth international conference on advanced computing & communication technologies*, 143–147.
- Waldert, S. (2016). Invasive vs. non-invasive neuronal signals for brain-machine interfaces: Will one prevail? *Frontiers in neuroscience*, 10, 189807.
- Weber, E., Köberl, A., Frank, S., & Doppelmayr, M. (2011). Predicting successful learning of smr neurofeedback in healthy participants: Methodological considerations. *Applied psychophysiology and biofeedback*, 36, 37–45.
- Wittevrongel, B., Holmes, N., Boto, E., Hill, R., Rea, M., Libert, A., Khachatrian, E., Bowtell, R., Brookes, M. J., & Van Hulle, M. M. (2021). Optically pumped magnetometers for practical meg-based brain-computer interfacing. *Brain-Computer Interface Research: A State-of-the-Art Summary* 10, 35–46.
- Wolf, S. L., Winstein, C. J., Miller, J. P., Taub, E., Uswatte, G., Morris, D., Giuliani, C., Light, K. E., Nichols-Larsen, D., EXCITE Investigators, f. t., et al. (2006). Effect of constraint-induced movement therapy on upper extremity function 3 to 9 months after stroke: The excite randomized clinical trial. *Jama*, 296(17), 2095–2104.
- Ying, X. (2019). An overview of overfitting and its solutions. *Journal of physics: Conference series*, 1168, 022022.
- Zerfowski, J., Sander, T., Tangermann, M., Soekadar, S., & Middelmann, T. (2021). Real-time data processing for brain-computer interfacing using optically pumped magnetometers. *International Journal of Bioelectromagnetism*, 23(2).
- Zerfowski, J. (2022). Optically pumped magnetometers for a brain-computer interface based on event-related desynchronization.
- Zrinzo, L., Foltynie, T., Limousin, P., & Hariz, M. I. (2012). Reducing hemorrhagic complications in functional neurosurgery: A large case series and systematic literature review. *Journal of neurosurgery*, 116(1), 84–94.
- Zubarev, I., Zetter, R., Halme, H.-L., & Parkkonen, L. (2019). Adaptive neural network classifier for decoding meg signals. *NeuroImage*, 197, 425–434.

*Characterization and Classification of Finger Movement-Related Brain Activity using  
Optically Pumped Magnetometers*

# Annex

## .1 Availability of the Source Code

All code used for preprocessing, analysis and classification of the data can be found in the following repository: <https://github.com/MarIniOnz/opm-thesis>. It contains the following files and folders:

- **readme.md**: Readme file containing the structure of the repository.
- **Makefile**: File containing a set of directives used with the *make* command line utility to automate the build process of a project. It includes commands for compiling code, installing dependencies, running tests, and formatting the files in the repository.
- **readme.md**: Readme file containing the structure of the repository.
- **pyproject.toml**: This file specifies the build system requirements for the Python project. It is used to define settings such as the package metadata, dependencies, and compatible versions.
- **setup.py**: A setup script for the package. This particular script specifies that the package is named *opm\_ thesis* and includes all sub-packages within the *opm\_ thesis* directory .
- **requirements.txt**: This file lists the dependencies for the Python project, specifying exact versions to ensure consistent environments.
- **master\_thesis.pdf**: The Master Thesis pdf-file (this one).
- **notebooks**: Folder containing the notebooks that created the figures and tables of the thesis.
- **opm\_thesis** Folder containing all the files to pre-process, analyze and classify the data.

The data used in the study has not been released to the public, but could be provided upon request.

## .2 Extra Figures

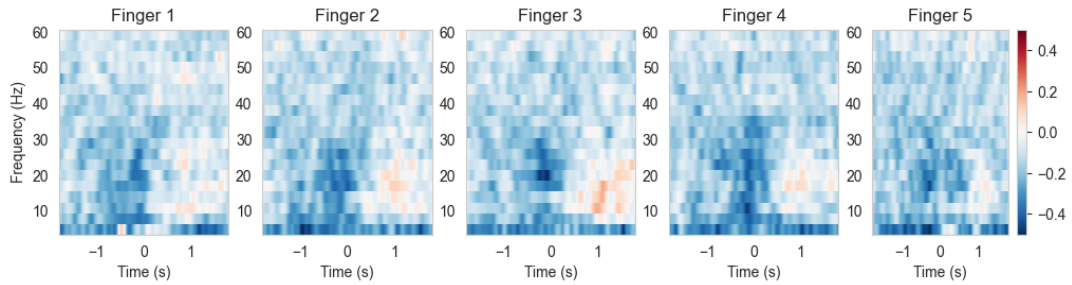


Figure .1: **Average TFR for different states for HI[X] channel.** Plots depicting the TFR of the center channel HI[X] averaged over trials pertaining to a different state. Time equals zero represents the button press.

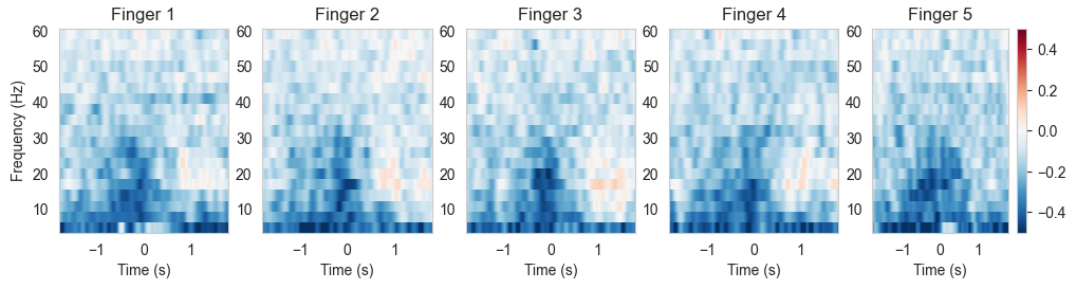
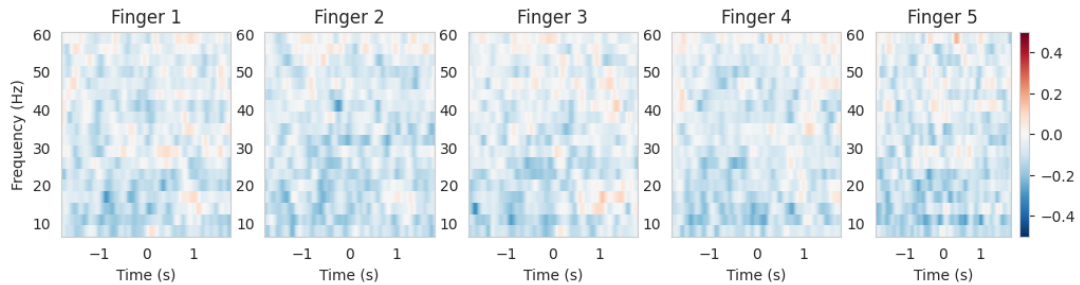
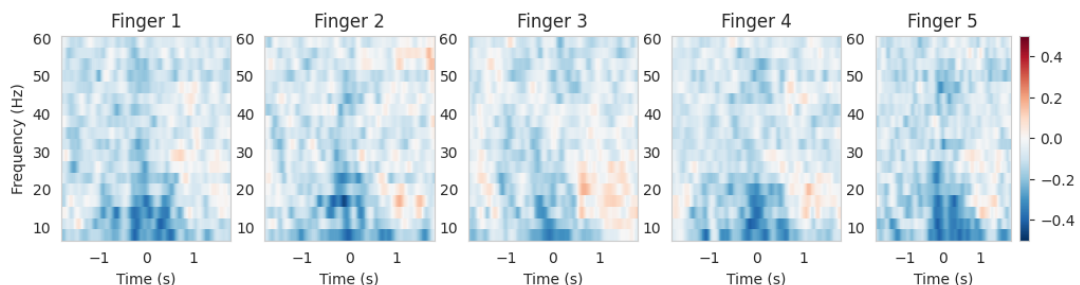


Figure .2: **TFR for different states for FW[X] channel.** Plots depicting the TFR of the center channel FW[X] averaged over trials pertaining to a different state. Time equals zero represents the button press.

*Characterization and Classification of Finger Movement-Related Brain Activity using  
Optically Pumped Magnetometers*



**Figure .3: Average TFR for different states for FY[Y] channel.** Plots depicting the TFR of the center channel FY[Y] averaged over trials pertaining to a different state. Time equals zero represents the button press.



**Figure .4: TFR for different states for HQ[Z] channel.** Plots depicting the TFR of the center channel HQ[Z] averaged over trials pertaining to a different state. Time equals zero represents the button press.